

4-2019

Simulation of T2 MRI Relaxation Enhancement by Magnetic Nanoparticles

Yahia Adeeb Tawfiq Hamdan

Follow this and additional works at: https://scholarworks.uaeu.ac.ae/phys_theses



Part of the [Physics Commons](#)

Recommended Citation

Tawfiq Hamdan, Yahia Adeeb, "Simulation of T2 MRI Relaxation Enhancement by Magnetic Nanoparticles" (2019). *Physics Theses*. 3.

https://scholarworks.uaeu.ac.ae/phys_theses/3

This Thesis is brought to you for free and open access by the Physics at Scholarworks@UAEU. It has been accepted for inclusion in Physics Theses by an authorized administrator of Scholarworks@UAEU. For more information, please contact fadl.musa@uaeu.ac.ae.

4-2019

Simulation of T2 MRI Relaxation Enhancement by Magnetic Nanoparticles

Yahia Adeeb Tawfiq Hamdan

Follow this and additional works at: https://scholarworks.uaeu.ac.ae/phys_theses



Part of the [Physics Commons](#)

Recommended Citation

Tawfiq Hamdan, Yahia Adeeb, "Simulation of T2 MRI Relaxation Enhancement by Magnetic Nanoparticles" (2019). *Physics Theses*. 3. https://scholarworks.uaeu.ac.ae/phys_theses/3

This Thesis is brought to you for free and open access by the Physics at Scholarworks@UAEU. It has been accepted for inclusion in Physics Theses by an authorized administrator of Scholarworks@UAEU. For more information, please contact fadl.musa@uaeu.ac.ae.



جامعة الإمارات العربية المتحدة
United Arab Emirates University

United Arab Emirates University

College of Science

Department of Physics

SIMULATION OF T_2 MRI RELAXATION ENHANCEMENT BY
MAGNETIC NANOPARTICLES

Yahia Adeeb Tawfiq Hamdan

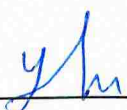
This thesis is submitted in partial fulfillment of the requirements for the degree of
Master of Science in Physics

Under the Supervision of Professor Bashar Afif Issa

April 2019

Declaration of Original Work

I, Yahia Adeeb Tawfiq Hamdan, the undersigned, a graduate student at the United Arab Emirates University (UAEU), and the author of this thesis entitled “*Simulation of T_2 MRI Relaxation Enhancement by Magnetic Nanoparticles*”, hereby, solemnly declare that this thesis is my own original research work that has been done and prepared by me under the supervision of Professor Bashar Afif Issa, in the College of Science at UAEU. This work has not previously been presented or published, or formed the basis for the award of any academic degree, diploma or a similar title at this or any other university. Any materials borrowed from other sources (whether published or unpublished) and relied upon or included in my thesis have been properly cited and acknowledged in accordance with appropriate academic conventions. I further declare that there is no potential conflict of interest with respect to the research, data collection, authorship, presentation and/or publication of this thesis.

Student's Signature: 

Date: 9-5-2019

Approval of the Master Thesis

This Master Thesis is approved by the following Examining Committee Members:

- 1) Advisor (Committee Chair): Prof. Saleh Thaker Mahmoud

Title: Professor

Department of Physics

College of Science

Signature _____



Date 23/04/2019

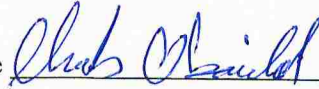
- 2) Member: Prof. Ihab Obaidat

Title: Professor

Department of Physics

College of Science

Signature _____



Date 23/04/2019

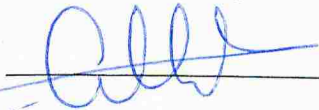
- 3) Member (External Examiner): Prof. Gaffar Attaelmanan

Title: Professor

Department of Applied Physics and Astronomy

Institution: University of Sharjah, UAE

Signature _____



Date 24/4/2019

Copyright © 2019 Yahia Adeeb Tawfiq Hamdan
All Rights Reserved

Advisory Committee

1) Advisor: Prof. Bashar Afif Issa

Title: Professor

Department of Medical Diagnostic Imaging

College of Health Sciences

Institution: University of Sharjah, UAE

2) Co-advisor: Prof. Saleh Thaker Mahmoud

Title: Professor

Department of Physics

College of Science

Abstract

The effect of high concentration of magnetic nanoparticles (MNP) on Magnetic Resonance Imaging MRI transverse relaxation rates ($R_2=1/T_2$ and $R_2^*=1/T_2^*$) was studied using Monte Carlo (MC) simulations. Theoretical models assume that particles occupy a small volume fraction of the sample space. This work aims to test if available models based on Motional Averaged (MAR) and Static Dephasing Regimes (SDR) can still represent relaxation rates at large volume fractions. Furthermore, echo-time effects, were tested on both gradient-echo and spin-echo sequences in order to examine if diffusion is involved. Findings will clarify if models need to be modified to take account of high particle concentration. This is especially important for application involving clustering of nanoparticles inside tissues or being trapped inside cells. Another important area is relaxation due to MNP administered through vesicles as a carrier medium. This is important to understand the relaxation mechanism caused by MNP in order to improve their design process.

Keywords: Magnetic nanoparticles, transverse relaxation, motional averaged, static dephasing, gradient-echo, spin-echo, clustering of nanoparticles.

Title and Abstract (in Arabic)

محاكاة ازدياد معامل الاسترخاء الثاني في الرنين المغناطيسي بوجود الجسيمات النانوية المغناطيسية

الملخص

تمت دراسة تأثير التركيز العالي للجسيمات النانوية المغناطيسية (MNPs) على معدلات الاسترخاء المستعرضة (transverse relaxation rates) للتصوير بالرنين المغناطيسي ($R_2=1/T_2$ و $R_2^*=1/T_2^*$) باستخدام محاكاة مونتني كارلو (MC). تفترض النماذج النظرية أن الجسيمات تشغل جزءاً حجمياً (volume fraction) صغيراً من مساحة العينة. تهدف هذه العمل الأطروحة إلى اختبار ما إذا كانت النماذج المتاحة القائمة على أساس أنظمة المعدلات الحركية (motional averaged regime MAR) وفقدان الأطوار السكونية (static dephasing regime SDR) يمكن أن تستمر في وصف معدلات الاسترخاء عند الأجزاء الحجمية الكبيرة. علاوة على ذلك، تمت دراسة تأثير زمن الصدى (echo time) على صدى الانحدار (gradient-echo) و صدى الغزل (spin-echo)، للتحقق عما إذا كان الانتشار متضمناً. ستوضح النتائج ما إذا كان يجب تعديل النماذج لمراعاة تركيز الجسيمات العالي، وهو أمر مهم بشكل خاص للتطبيقات التي تنطوي على تجميع المغناطيسية داخل الأنسجة أو المحاصرة داخل الخلايا. تطبيق آخر مهم هو الاسترخاء بسبب الجسيمات النانوية المغناطيسية التي تدار من خلال الحويصلات كوسيط الناقل. هذا مهم لفهم آلية الاسترخاء التي تسببها المغناطيسية من أجل تحسين عملية التصميم الخاصة بها.

مفاهيم البحث الرئيسية: الجسيمات النانوية المغناطيسية، معدلات الاسترخاء المستعرضة،

أنظمة المعدلات الحركية، أنظمة فقدان الأطوار السكونية، زمن الصدى.

Acknowledgements

I would like to thank my thesis advisors Prof. Bashar Issa and Prof. Saleh Thaker for their steady support and enthusiasm throughout this research effort. Our discussions of research ideas allowed me to come up with this unique idea that crosses between many different hot areas of research and involves a lot of topics that greatly strengthen my academic knowledge. I sincerely thank my family and friends for their enormous support and motivation that they have provided me. This motivation helped in bringing the best out of me towards my educational and professional progress.

Dedication

To my beloved ones

Table of Contents

Title	i
Declaration of Original Work	ii
Copyright	iii
Advisory Committee	iv
Approval of the Master Thesis	v
Abstract	vii
Title and Abstract (in Arabic)	viii
Acknowledgements	ix
Dedication	x
Table of Contents	xi
List of Tables.....	xiii
List of Figures	xiv
List of Abbreviations.....	xv
Chapter 1: Introduction	1
1.1 Overview	1
1.2 Statement of the problem	1
1.3 Purpose of the study	2
1.4 Limitations of the study	2
Chapter 2: Theory	3
2.1 Nuclear Magnetic Resonance Overview	3
2.1.1 A brief history of NMR.....	3
2.1.2 The phenomenon of NMR.....	3
2.1.3 NMR Relaxation	4
2.2 Factors affecting MRI image contrast.....	5
2.2.1 T ₁ and T ₂ weighted image	6
2.2.2 MRI Contrast Agents	7
2.2.3 Superparamagnetic Nanoparticles	8
2.3 Motional Regimes	8
2.3.1 Motional Averaging Regime	9
2.3.2 Static Dephasing Regime	10
2.3.3 Echo Limited Regime.....	10
Chapter 3: Methods	12
3.1 Numerical Simulation	12
3.2 The boundary conditions.....	17

3.3 Calculating R_2 and R_2^*	18
Chapter 4: Results	20
4.1 Validation	20
4.2 The effect of increasing volume fraction	22
4.3 The effect of changing the number of magnetic nanoparticles	25
4.4 Motional Regimes	27
4.4.1 MAR (R=10 nm)	27
4.4.2 SDR/ELR (R=240 nm)	27
4.4.3 The saturation effect	30
4.5 The effect of increasing volume fraction on R_2^* at different τ_{CP} values	30
4.6 The effect of increasing volume fraction on R_2 and at different τ_{CP} values	31
4.7 The effect of increasing τ_{CP} on R_2^* for different volume fractions	34
4.8 The effect of increasing τ_{CP} on R_2 for different volume fractions	35
4.9 The effect of increasing τ_{CP} on the slope of (R_2 and R_2^* vs. the volume fraction)	36
4.10 3D Graphs	38
Chapter 5: Discussion and Conclusion	40
5.1 The transverse relaxation at high concentration	40
5.2 The effect of the echo time on transverse relaxation on the 10 nm SPIONs	41
5.3 The effect of the echo time on transverse relaxation on the 240 nm	44
5.4 Conclusion	46
References	48

List of Tables

Table 1: The values of the relaxation vs. f slopes and their R-squared values for 240 nm SPIONs	42
Table 2: The values of the relaxation vs. f slopes and their R-squared values for 10 nm SPIONs	43

List of Figures

Figure 1: Random walk of a spin going through 100 jumps.....	12
Figure 2: Plot of Bz at plane (x, y) of $(z = 0)$ of a MNP which has a radius of 10 nm and placed at the center: $(x, y, z) = 0$	15
Figure 3: The isofield lines around a single MNP in the plane $(z=0)$	16
Figure 4: R_2^* vs. τD for all motional regimes	21
Figure 5: R_2 vs. τD for all motional regimes	22
Figure 6: R_2^* values plotted vs. volume fraction.....	24
Figure 7: R_2 values plotted vs. volume fraction.....	24
Figure 8: The effect of increasing the number of the particles on R_2	26
Figure 9: The effect of increasing the number of the particles on R_2^*	26
Figure 10: Values of \ln of the accumulated phase of the spins in both SE and GE at volume fraction of 1.0×10^{-6}	28
Figure 11: The natural logarithm of the phases accumulated by the 4000 spins in random walk around 50 SPIONs of radii 240 nm plotted vs. time. The parameters in each subplot are (a) $\tau_{CP} = 1.0 \times 10^{-4}$ s; $f = 5.0 \times 10^{-5}$ (b) $\tau_{CP} = 1.0 \times 10^{-3}$ s; $f = 5.0 \times 10^{-5}$; (c) $\tau_{CP} = 1.0 \times 10^{-3}$ s; $f = 5.0 \times 10^{-4}$; (d) $\tau_{CP} = 1.0 \times 10^{-3}$ s; $f = 1.0 \times 10^{-5}$	29
Figure 12: R_2^* vs. volume fraction at different the echo time $R=10$ nm	31
Figure 13: R_2^* values plotted against volume fraction for 50 SPIONs of 240 nm radii	31
Figure 14: R_2 values plotted against volume fraction for 50 SPIONs of 240 nm radii	32
Figure 15: R_2 values plotted against volume fraction for 50 SPIONs of 10 nm radii	33
Figure 16: R_2^* values plotted against volume fraction for 50 SPIONs of 240 nm radii	34
Figure 17: R_2^* values plotted against volume fraction for 50 SPIONs of 10 nm.....	35
Figure 18: R_2 values plotted against volume fraction for 50 SPIONs of 10 nm.....	36
Figure 19: R_2 values plotted against volume fraction for 50 SPIONs of 240 nm.....	36
Figure 20: Comparing Slopes of $(R_2^*$ vs. $f)$ and $(R_2$ vs. $f)$ vs. τ_{CP} ; $R=10$ nm.....	37
Figure 21: Comparing Slopes of $(R_2^*$ vs. $f)$ and $(R_2$ vs. $f)$ vs. τ_{CP} ; $R=240$ nm.....	38
Figure 22: 3D Representation of R_2 and R_2^* against volume fraction and echo time.....	39

List of Abbreviations

CA	Contrast agent
ELR	Echo limited regime
GR	Gradient echo
HPC	High performance computer
MAR	Motional averaging regime
MNP	Magnetic nanoparticles
MRI	Magnetic resonance imaging
NMR	Nuclear magnetic resonance
R_2	Transverse relaxation rate coming from spin-spin interaction
R_2^*	Total transverse relaxation rate including the contribution from field gradient
RF	Radio frequency
SDR	Static dephasing regime
SE	Spin echo
SNR	Signal-to-noise ratio
SPIOs	Superparamagnetic iron oxide nanoparticles
TE	Echo time
$\Delta\phi$	The accumulated phase by the spins
γ	Gyromagnetic ratio

Chapter 1: Introduction

1.1 Overview

Magnetic Nanoparticles (MNPs) are used as Magnetic Resonance Imaging (MRI) Contrast Agents (CA) due to their large magnetic moment per unit mass relative to Gd-chelate complexes. The large magnetic field gradients created around the MNPs shorten transverse relaxation times of protons by enhancing spin dephasing very effectively rendering these MNPs as MRI negative CA.

MRI is widely applied in medicine today to image the anatomy of the body's internal organs. MRI has an advantage over the other medical imaging techniques that it does not include ionizing radiation, which makes MRI a non-invasive imaging method. However, the image contrast depends on certain factors, some of these factors are the transverse relaxation rates which are the reciprocal of the relaxation times ($R_2=1/T_2$ or $R_2^*=1/T_2^*$).

This work examines transverse relaxation behavior when the MNPs volume fraction becomes large, and compares MC simulation predictions with the existing models. The disagreement between them is examined as a function of particle volume fraction, particle size, and echo-time under the different motional regimes.

1.2 Statement of the problem

Theoretical models which are present today are limited to very small volume fractions. However, MNPs may agglomerate due to natural sedimentation effects and large magnetic dipolar interactions. This can ensue under in-vivo environment or heating as in hyperthermia conditions, where the creation of larger particles increases the concentration of MNPs beyond those anticipated originally rendering the

accuracy of quantitative experiments in question. Therefore, Monte Carlo (MC) simulations were used in this work to study the effect of large volume fractions of MNPs on R_2 and R_2^* .

1.3 Purpose of the study

This research aims at using Monte Carlo (MC) simulations in order to study the effect of increasing volume fractions of superparamagnetic iron oxide SPIONs magnetic nanoparticles on R_2 and R_2^* . It aims also to test if the simulation values agree with the theoretical models which were developed under the condition of small volume fraction and whether the data under the condition of increasing volume fraction can be modeled parametrically.

1.4 Limitations of the study

The work in this study would not be possible without the use of High Performance Computer HPC. However, obtaining the relaxation rate values for MNPs of radii below 10 nm required excessive calculations and may require longer time than the maximum assigned HPC wall time. The range of the echo time is another limitation of this study as longer echo time requires excessive calculations for the very small particles. Moreover, the signal may die out for larger values of the echo time which could not put the small MNPs of 10 nm radii under the same echo-time range with the MNPs of 240 nm radii.

Chapter 2: Theory

2.1 Nuclear Magnetic Resonance Overview

2.1.1 A brief history of NMR

Nuclear magnetic resonance (NMR) was discovered by Isidor Isaac Rabi who received Nobel Prize in Physics in 1944. Nuclear magnetic resonance was observed in bulk matter by Felix Bloch and Purcell who worked independently [1]. NMR is the basic principle for what is known today as Magnetic Resonance Imaging (MRI). The first MRI image was published in Nature in 1973 by Lauterbur. Prof. Peter Mansfield produced the first image of a human body part in 1977. MRI was approved for clinical use in 1985 [2, 3].

2.1.2 The phenomenon of NMR

Nuclear Magnetic Resonance is a physical phenomenon that describe the absorption and emission of electromagnetic energy in the presence of an external static magnetic field B_0 . Nuclei will precess around the direction of the applied magnetic field at a frequency called Larmor frequency and described by Larmor equation.

$$\omega_0 = \gamma B_0 \quad (1)$$

Where ω_0 is the angular precession frequency, γ is the gyromagnetic ratio of the nucleus, and B_0 is the strength of the external static magnetic field.

Radiofrequency (RF) pulse, which is a term for the oscillating magnetic field

(B_1) that is oscillating at the Larmor frequency, is able to flip the bulk magnetization of nuclei an angle (α) away from its thermal equilibrium direction. Just after the flip and turning off B_1 , the nuclei will start to dephase in the transverse plane (the xy-plane), which is perpendicular to the static magnetic field (B_0), and the net longitudinal magnetization will return to its thermal equilibrium position in the longitudinal direction (z-direction) parallel to the static magnetic field as long as the nuclei remain under the effect of the static magnetic field only [4].

Only nuclei with non-zero quantum spin are NMR active. This study will consider protons in water molecules 1H which have spin (1/2).

2.1.3 NMR Relaxation

Two relaxation processes are present after excitation, and they are independent of each other. T_1 (spin-lattice) indicates the characteristic time for the recovery of ~63% of the longitudinal magnetization towards the static magnetic field (B_0). T_2 (spin-spin), indicates the decay of ~63% of the magnetization in the plane transverse to the static magnetic field keeping ~37% of magnetization in the transverse plane [4].

The longitudinal magnetization after a 90° RF excitation pulse as a function of time is described by Equations (2) [4].

$$M_z = M_0(1 - e^{-t/T_1}) \quad (2)$$

Where M_z is the longitudinal magnetization after the 90° excitation RF pulse, M_0 is the thermal equilibrium value of M_z in the presence of the static magnetic field only, and T_1 is the spin-lattice relaxation time. The transverse magnetization

component M_{xy} is described by Equation (3).

$$M_{x,y} = M_0 e^{-t/T_2}. \quad (3)$$

Where $M_{x,y}$ is the magnetization in a plane perpendicular to the static magnetic field (transverse direction) and T_2 is the spin-spin relaxation time.

Equation (4) is known as Bloch equation and describes the nuclear magnetic resonance phenomena.

$$\frac{d\mathbf{M}}{dt} = \gamma \mathbf{M} \times \mathbf{B}_{eff} - \frac{M_x \hat{i} + M_y \hat{j}}{T_2} - \frac{(M_z - M_0) \hat{k}}{T_1} \quad (4)$$

Where \mathbf{M} is the nuclear net magnetization vector rotating around the static magnetic field at Larmor frequency, \mathbf{B}_{eff} is the vector sum of \mathbf{B}_z in the rotating frame and \mathbf{B}_1 , and (M_x, M_y, M_z) are the components of the magnetization vector in the rotating frame.

After the excitation using 90° RF pulse, \mathbf{B}_{eff} will become zero and the first term in Equation (4) drops. Equations (2) and (3) will represent the solution to Bloch equation in this case [4].

2.2 Factors affecting MRI image contrast

MRI is a technique that uses the NMR signal to produce an image. It has advantage of its ability to excite certain MRI active nuclei based on their gyromagnetic ratios in presence of a static magnetic field, RF coil and gradient coil.

The image contrast depends on the experiment design (The strength of the static magnetic field B_0 , pulse sequence, time to repeat (TR) which is the time between two successive RF pulses) and depends on the sample parameters as well

such as (spin-lattice relaxation time T_1 , spin-spin relaxation time T_2 , proton density, etc) [4, 5].

2.2.1 T_1 and T_2 weighted image

In order to get T_1 -weighted image short (TR) is needed along with a short echo time (TE) which is the time between the excitation pulse and the peak of the signal. On the other hand, long TR and long TE will be needed to get T_2 -weighted image.

Furthermore, the magnetic field need to be homogeneous. Otherwise, the transverse relaxation time T_2^* will be smaller than T_2 as the inhomogeneity of the magnetic field or the chemical environment, causes faster dephasing. The relaxation time in the presence of a magnetic field inhomogeneity is denoted by T_2^* and described by Equation (5) [4].

$$\frac{1}{T_2^*} = \frac{1}{T_2} + \frac{1}{T_{inh}} \quad (5)$$

The coil that produces the RF pulse can also detect an induced RF electromagnetic signal originating from the relaxation process. This signal is characterized by T_2^* and it is used to produce the MR image.

To measure T_2 , which reflects the actual spin-spin relaxation time, phases must be rephased. This is called spin-echo and achieved by applying 180° RF pulse after 90° RF pulse. This was discovered by Hahn in 1950 when he applied two successive 90° RF pulses and obtained a signal [6].

Carr and Purcell (CP) explained the advantage of using 180° RF refocusing pulses after the first 90° excitation pulse which was applied at time τ_{CP} [2].

The Carr–Purcell–Meiboom–Gill (CPMG) pulse sequence [7] is an enhanced method similar to the Curl-Purcell method with several 180° RF pulses after the first 90° RF pulse. It is only different from Carr-Purcell method in the phase of the 180° RF pulses.

Just after the excitation, spins will start to dephase and signal will decay in the transverse direction. A 180° RF pulse will be applied and spins will start to rephase again. This is equivalent to start the experiment again, but the signal will be less due to spin-spin relaxation. Several 180° RF pulses may be applied several times during the experiment, the time between each consecutive echoes TE is equal to ($2\tau_{CP}$). The echo signal is sampled at ($t= \tau_{CP}, 3\tau_{CP}, 5\tau_{CP}, \dots$). After n-repetitions, the echoes will be in exponential decay with a time constant (T_2). CPMG is excessively used in NMR experiments [4].

2.2.2 MRI Contrast Agents

MRI contrast agent (CA) is a substance that is added to a sample prior to getting the MRI scan. The aim of using CA is to increase the difference in the relaxation times between the nearby spins of the sample and the surrounding which have different concentration of the CA or no CAs at all. This would affect the intensity of MRI signal and consequently enhance MRI image contrast.

Contrast agents are classified based on their effect on T_1 and T_2 to positive and negative contrast agents. Positive contrast agents decrease T_1 relaxation time and affects T_1 -weighted image by making it brighter. An examples of positive contrast agents are complexes of the lanthanide gadolinium (III) (Gd). In contrast, negative contrast agents reduce mainly T_2 and T_2^* , which would cause darkness in contrast

enhanced tissues. Negative contrast agents act as positive contrast agents in T₁-weighted images as they shorten T₁ relaxation time and cause brightness in the image. Superparamagnetic iron oxide (SPIONs) is classified as a negative contrast agent [5, 8] .

2.2.3 Superparamagnetic Nanoparticles

Superparamagnetic nanoparticles have high magnetic susceptibilities. Magnetic susceptibility is a dimensionless physical quantity that represents the slope of linear graph between the externally applied magnetic field as independent variable and induced magnetization as dependent variable. Increasing the magnetic field would have substantial increase in magnetization. As the magnetic field of MNP falls off as $(1/r^3)$ where r represents the distance from the center of the MNP, superparamagnetic nanoparticles would have relatively high magnetic field gradients affecting T₂ and T₂*. These magnetic field gradients will have an effect in dephasing the magnetic moments of the proton. Therefore, superparamagnetic nanoparticles are considered as useful contrast agents.

2.3 Motional Regimes

Theoretical models of transverse relaxation of protons are classified into regimes based on a parameter known as the dynamic or diffusion time τ_D , which is given by Equation (6).

$$\tau_D = \frac{R^2}{D} \quad (6)$$

Where R is the radius of the particle and D is the diffusion coefficient. τ_D reflects the time required for a spin to diffuse a distance $\sqrt{2}R$ in any direction in the three-dimensional space.

If the condition $\tau_D \ll 1/\omega_r$ is valid (where ω_r is the Larmor frequency experienced by the proton at the equator of the MNP), then the Motional Averaging Regime (MAR) will apply and both R_2 and R_2^* are equal to each other and increase linearly with both τ_D and the volume fraction. This increase is independent of the Spin-Echo (SE) time τ_{CP} used.

Increasing the size of the MNPs would increase the value τ_D . If the value of τ_D satisfies the condition ($\tau_D \gg 1/\omega_r$), Static Dephasing Regime (SDR) will apply and the value of R_2^* reach its maximum and becomes independent of the MNPs sizes and accordingly independent from τ_D .

For large MNPs satisfying the condition ($\tau_D > 2\tau_{CP}$), a new regime applies called the Echo Limited Regime (ELR). In this regime partial refocusing occurs under the effect of 180° RF pulses and R_2 starts decreasing with increasing τ_D .

2.3.1 Motional Averaging Regime

For the small MNPs satisfying the condition ($\tau_D \ll 1/\omega_r$), spins are considered in motion around the MNPs and this is termed Motional averaging regime MAR. This regime is governed by the outer sphere theory [9, 10] .

The diffusion time is short, the spins are considered to diffuse efficiently around the MNPs and the relaxation would depend on the particle's size and the diffusion constant of the medium (D).

As the diffusion time increases, the relaxation rate will increase. The relaxation rates will be given by: [9-12].

$$R_2 = R_2^* = \left(\frac{16}{45}\right) \omega_r^2 f \tau_D \quad (7)$$

2.3.2 Static Dephasing Regime

For larger MNPs satisfying the condition $\tau_D \gg 1/\omega_r$, the regime is termed Static Dephasing Regime SDR and the relaxation will be independent of both the diffusion constant and MNP size. The theory in the static SDR does not quantify the value of R_2 . Only the value of R_2^* is described. R_2^* and it is given by Equation (8) [13, 14].

$$R_2^* = \left(\frac{2\pi}{3\sqrt{3}}\right) \omega_r f \quad (8)$$

2.3.3 Echo Limited Regime

The Echo Limited Regime (ELR) becomes applicable where the refocusing pulses become efficient, i.e. where some of the transverse magnetization is recovered after 180° pulse if the superparamagnetic nanoparticles are large enough to satisfy the condition ($\tau_D > 2\tau_{CP}$), then R_2 will be described by Equation (9) [10, 15, 16].

$$R_2 = \frac{7.2 f D x^{\frac{1}{3}} (1.52 + fx)^{5/3}}{4R^2} \quad (9)$$

Where $x = \omega_r \tau_{CP}$. The value for R_2 in this regime will decrease by increasing τ_D , and will be affected by changing the echo times.

Chapter 3: Methods

3.1 Numerical Simulation

Monte Carlo simulation is used to obtain numerical results for the transverse relaxation rates ($R_2=1/T_2$) and ($R_2^* = 1/T_2^*$). The water molecules, which contain spin (1/2) protons, are considered in random walk in the sample. Figure 1 shows a trajectory of a spin in a random walk moving 100 steps in the 3D-space. The voxel which represents the sampling space is considered cubic.

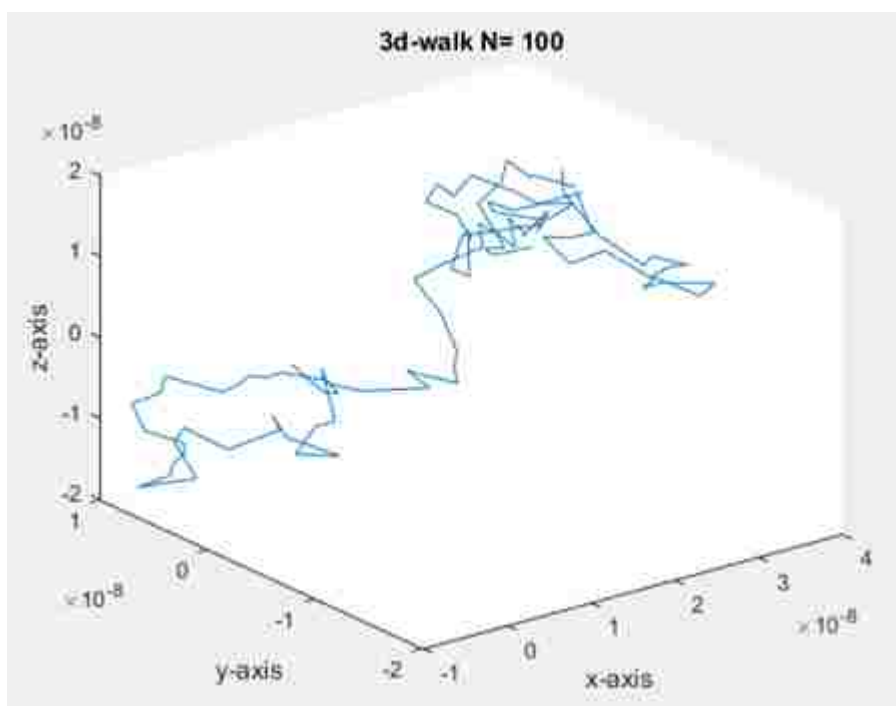


Figure 1: Random walk of a spin going through 100 jumps

This study utilizes a Matlab code developed by Dr. Bashar Issa at UAEU. 4000 spins were considered in a random walk around magnetic nanoparticles which were randomly distributed over 40 spatial distributions in a cubic voxel (i.e. 40 arrangements of nanoparticles' positions in the 3-D space). The number of the spins

and the number of spatial distributions in the random walk are the optimum numbers for the code in terms of producing relaxation decay curves and acceptable SNR.

The transverse relaxation rates for Superparamagnetic Iron Oxides (SPIONs) magnetic nanoparticles were evaluated using High Performance Computer (HPC) for all the motional regimes.

The SPIONs are distributed within the cubic three-dimensional space and considered stationary. The 4000 spins start their walk from random positions and are not overlapping with the SPIONs. As the spins accumulate phase shift during their random walk. This phase shift is used to evaluate the transverse relaxation rates.

In order to evaluate R_2 using the MC simulation, CPMG pulse sequence was used which employs eight 180° RF refocusing pulses at odd multiples of half of the 180° RF pulse spacing τ_{CP} .

Between each two refocusing pulsed, spins go through a certain number jumps in random directions. Each spin is allowed to move a distance of $\sqrt{2D\Delta t}$ in each jump, where D is the self-diffusion coefficient of water ($2.5 \times 10^{-9} \text{ m}^2/\text{s}$) at 25°C and Δt is the time for a spin to jump to its new position and is given by

$$\Delta t = \frac{2 \times \tau_{CP}}{\text{(number of jumps between the } 180^\circ \text{ RF pulses)}} \quad (10)$$

The number of jumps and τ_{CP} were chosen to optimize Δt which, in turn, would give a jump size near to two-thirds the radius of a single MNP, as this would effectively sample the magnetic field variation during the random walk.

As each spin reaches its new position, the magnitude of the total magnetic field (\mathbf{B}_z) originating from all the SPIONs along the direction of the static magnetic field (\mathbf{B}_0) would be evaluated. This value of (\mathbf{B}_z) is used to calculate the phase shift according to the relation [17]

$$\Delta\phi = \gamma B_z \Delta t \quad (11)$$

Where γ is the gyromagnetic ratio of the proton 1H which is equal to $2.675 \times 10^8 \text{ rad.s}^{-1}.T^{-1}$.

The SPIONs were considered as magnetic dipoles. The longitudinal component B_z of the magnetic field for each SPIONs of a single particle is classically given by the relation [18].

$$B_z(r, \theta) = \frac{\mu_0 M}{3} \left(\frac{R}{r}\right)^3 (3\cos^2\theta - 1) \quad (12)$$

Figure 2 below shows the magnetic field B_z for a single MNP placed at plane (x, y) of (z = 0)

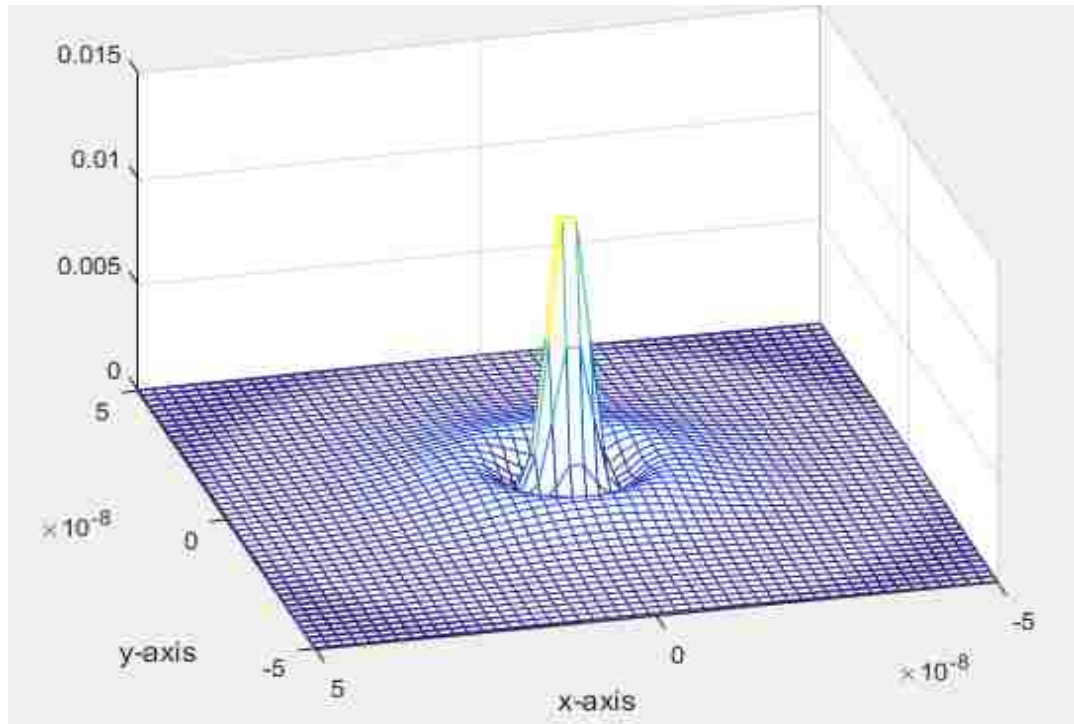


Figure 2: Plot of B_z at plane (x, y) of $(z = 0)$ of a MNP which has a radius of 10 nm and placed at the center: $(x, y, z) = 0$

Equation (12) can be used to visualize the isofield lines around each MNP as both $(r$ and $\theta)$ change, where r is the distance between the spin and the center of the MNP, and θ is the angle between the spins and the magnetization vector M in Figure 3.

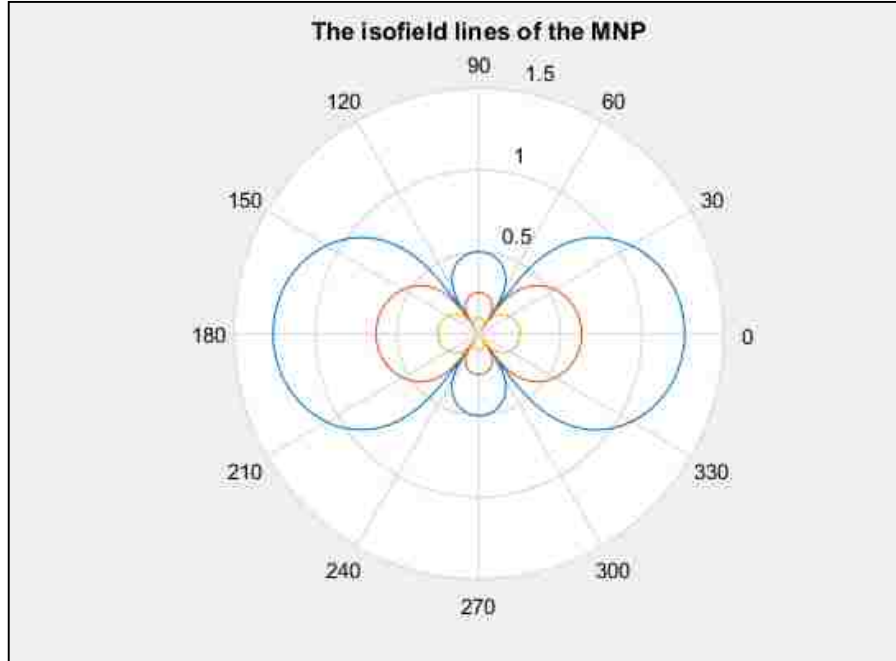


Figure 3: The isofield lines around a single MNP in the plane ($z=0$)

The frequency shift experienced by the spin at the equator of the MNP can be given by

$$\omega_r = \left| \gamma \times B(r = R, \theta = \frac{\pi}{2}) \right| = \frac{\mu_0 \gamma M}{3} \quad (13)$$

Where \mathbf{M} is the magnetization of the MNP, R is the radius of the MNP, μ_0 is the permeability which is equal to $4\pi \times 10^{-7} \text{H/m}$, θ is the azimuthal angle which is the angle between the position \mathbf{r} vector of the spin from the magnetization \mathbf{M} .

Equation (13) is used in the code to find the magnitude of the magnetization vector, which will be used in turn to calculate B_z and the frequency shift accumulated by the spins following each jump using Equation (11).

In order to get Spin-Echo relaxation rate, the phases are inverted at each 180° RF pulse, i.e. at $(3\tau_{CP}, 5\tau_{CP}, 7\tau_{CP}, 9\tau_{CP}, 11\tau_{CP}, 13\tau_{CP}, 15\tau_{CP})$, where τ_{CP} is half the 180° RF pulse spacing in CPMG pulse sequence.

Accumulated phase was calculated to evaluate the R_2 and the signal was sampled at $(2\tau_{CP}, 4\tau_{CP}, 6\tau_{CP}, 8\tau_{CP}, 10\tau_{CP}, 12\tau_{CP}, 14\tau_{CP}, 16\tau_{CP})$. The refocusing pulses were removed in Gradient echo calculation. Equation 14 [17] is used to evaluate the signal. The accumulated phases were substituted in Equation (14).

$$S(t) = \frac{1}{N_s} \sum_{n=1}^{N_s} e^{i\phi_n(t)} \quad (14)$$

Where ϕ_i is the phase of the n-th spin at time t, where N_s is the total number of spins which is 4000 in this study. The natural logarithm of the $S(t)$ was calculated, and exponential fitting was used to evaluate the values of R_2 and R_2^* .

3.2 The boundary conditions

- The spins will start their random walk from a random position in the voxel.
- The spins are not allowed to bypass the MNP, in case the jump is supposed to go through a MNP, the jump will be cancelled and new jump will be generated.

- Spins are not allowed to penetrate the SPIONs or the voxel which has a side described by Equation (15) [11].

$$s = \sqrt[3]{\frac{\sum_i \left(\frac{4\pi}{3}\right) R_i}{f}} \quad (15)$$

- The boundary condition of the surface is assumed to be periodic; In the case the spin has a jump that would penetrate the voxel from one side then the spin will be relocated in the voxel from the opposite side.

3.3 Calculating R_2 and R_2^*

The relaxation rates (R_2 and R_2^*) were found using monoexponential fitting of the sampled data for the 10 nm SPIONs. In certain cases, in which there are fast dephasing and slow dephasing zones, double exponential fitting was used. This was applied to the 240 nm SPIONs as the simulation results did not show single exponential behavior for the spin-echo. However, the gradient echo was single exponential for all of the particles' sizes.

Firstly, validation studies were run initially to ensure that the simulation code output was in agreement with the published results and theoretical models. The simulation was run for 20 sizes of SPIONs ranging between (5 nm and 400 nm). Figure 4 and Figure 5. The values obtained showed agreement with the theoretical models with the published studies [15, 19].

In each run, the number of SPIONs was 50 and the particles were of equal size. The echo time between each two 180° RF refocusing pulses was $(2.0 \times 10^{-5} \text{s})$.

High performance computer (HPC) was used to run all the simulations in this study. The first study was for low volume fraction ($f = 1.0 \times 10^{-6}$) of SPIONs in bulk water. The simulation was repeated for particles which have radii larger than 150 nm for another two echo times ($\tau_{CP} = 1.0 \times 10^{-4} s$) and ($\tau_{CP} = 5.0 \times 10^{-4} s$) in order to scan the R_2 values in Echo Limited Regime. The transverse relaxation rates ($R_2=1/T_2$) and ($R_2^* = 1/T_2^*$) were evaluated versus the varying particles' sizes for different plots in ELR.

The simulations results were validated under different number of particles (1, 10 and 50) SPIONs to check for the agreement with the theory (Figure 6 and Figure 7). The volume fraction was increased gradually from ($f = 1.0 \times 10^{-6}$) to ($f = 1.0 \times 10^{-3}$) to check if the agreement with the theory will continue at high volume fractions, and to investigate the effect of the number of the particles on the transverse relaxation rates ($R_2=1/T_2$) and ($R_2^* = 1/T_2^*$).

The behavior of R_2 and R_2^* vs. volume fraction is studied at different values of τ_{CP} for two case studies. The first case is for 50 particles of 10 nm radius, while the second case study investigates 50 particles of 240 nm radius, and obviously the two sizes scan both regimes of MAR and SDR. The range of τ_{CP} for the 10 nm particles was ($\tau_{CP} = 5.0 \times 10^{-8} s$) to ($\tau_{CP} = 5.0 \times 10^{-5} s$), while for the 240 nm particles was ($\tau_{CP} = 3.0 \times 10^{-5} s$) to ($\tau_{CP} = 1.0 \times 10^{-3} s$). For the volume fraction (f) the range was ($f = 1.0 \times 10^{-6}$) to ($f = 1.0 \times 10^{-3}$) for both particle sizes. The simulation was repeated multiple times and the error was estimated.

Chapter 4: Results

4.1 Validation

The results of the simulation transverse relaxation rates at low volume fraction ($f = 1.0 \times 10^{-6}$) showed agreement with the theoretical values and the published experimental results [17, 20, 21].

The first results obtained, as shown in Figure 4, were the validation results for the simulation and was run for 50 SPIONs under a volume fraction ($f = 1.0 \times 10^{-6}$) and echo-time ($\tau_{CP} = 1.0 \times 10^{-5}s$). ω_r was equal to ($3.4 \times 10^7 s^{-1}$), the diffusion times chosen were between ($\tau_D = 1.0 \times 10^{-8}s$) and ($\tau_D = 6.1 \times 10^{-5}s$) corresponding to SPIONs radii range between ($R=5.0$ nm and $R=400$ nm), as this would scan all the motional regimes.

R_2^* Simulation values increased linearly with increasing (τ_D) in MAR and showed agreement with motional averaging regime theoretical values (Equation (7)). As τ_D values increased and reached the SDR limit, R_2^* simulation values became τ_D independent and agreed with the constant value of the static dephasing regime theoretical values (Equation (8)).

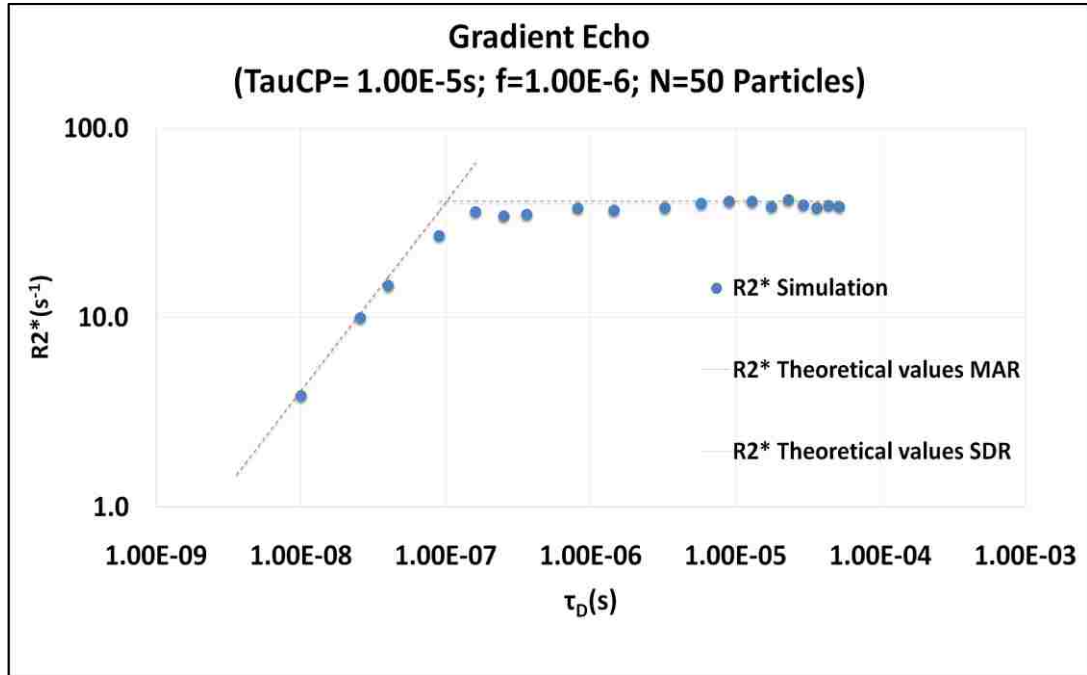


Figure 4: R_2^* vs. τ_D for all motional regimes

R_2 Relaxation rates (Figure 5) showed agreement with the theory for the small particles in MAR, where R_2 simulation values increased linearly and agreed with the theoretical values (Equation 7). Once the values of τ_D passed MAR limit, the values of R_2 relaxation rates kept increasing reaching a maximum, then decreased with increasing τ_D , in this intermediate region there is no theory present to quantify R_2 relaxation rates.

For values of τ_D , in Figure 5, between ($\tau_D = 1.3 \times 10^{-5} s$) and ($\tau_D = 6.1 \times 10^{-5} s$) which corresponds to SPIONs radii ranging between ($R=180$ nm and $R=400$ nm). Two more values of τ_{CP} were used ($\tau_{CP} = 1.0 \times 10^{-4} s$) and ($\tau_{CP} = 5 \times 10^{-4} s$). In the case of ($\tau_{CP} = 1.0 \times 10^{-4} s$), the minimum MNP radius at which the

relaxation could be evaluated using the simulation was (10 nm), due to the computational power limitation.

The results showed that R_2 values obtained from the simulation decreased by increasing τ_D and increasing with increasing values of τ_{CP} . This agrees with the published results [15].

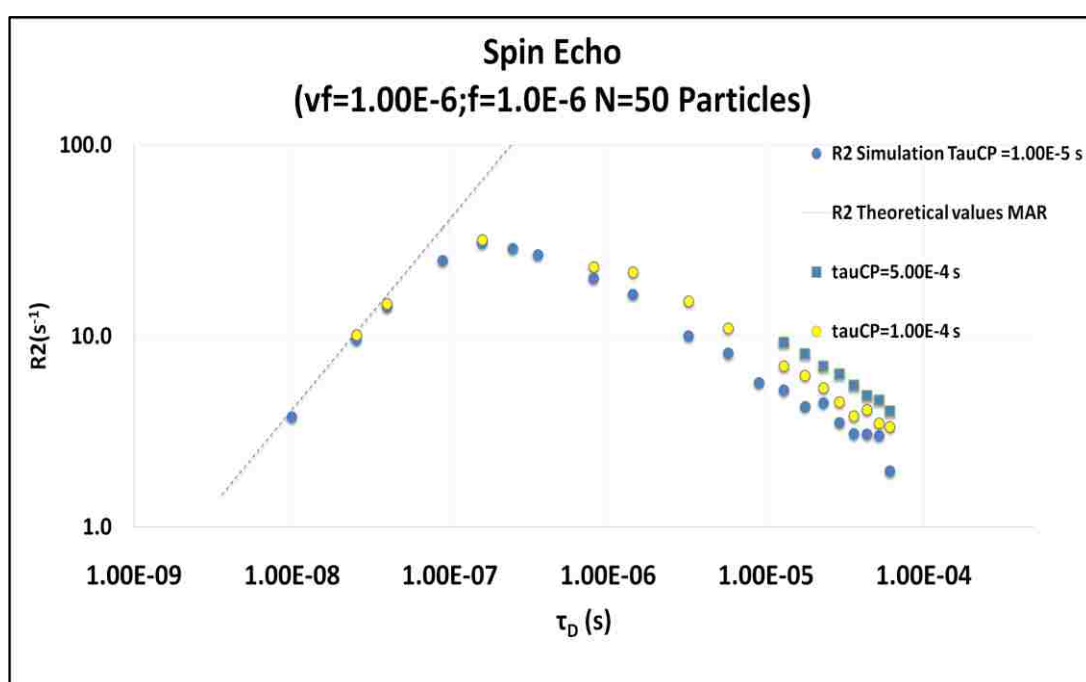


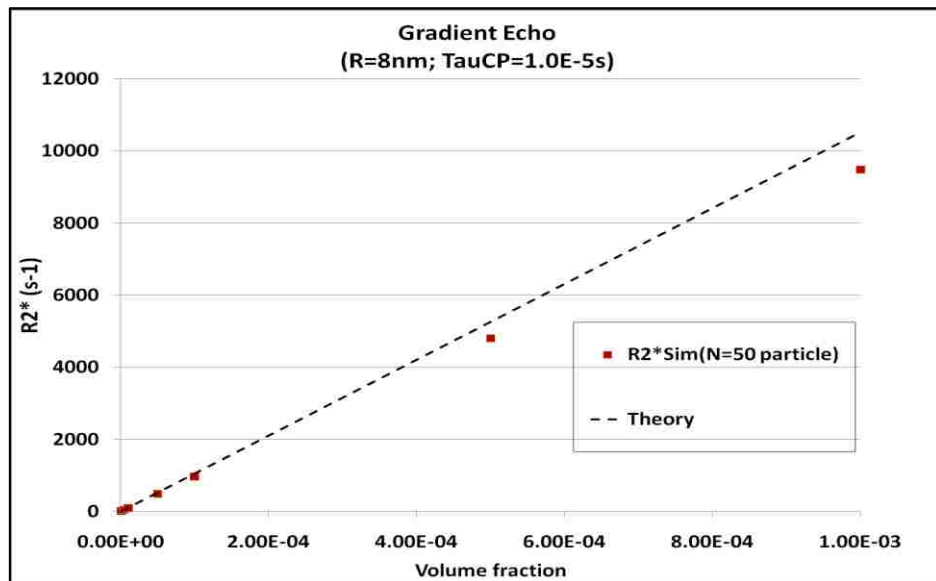
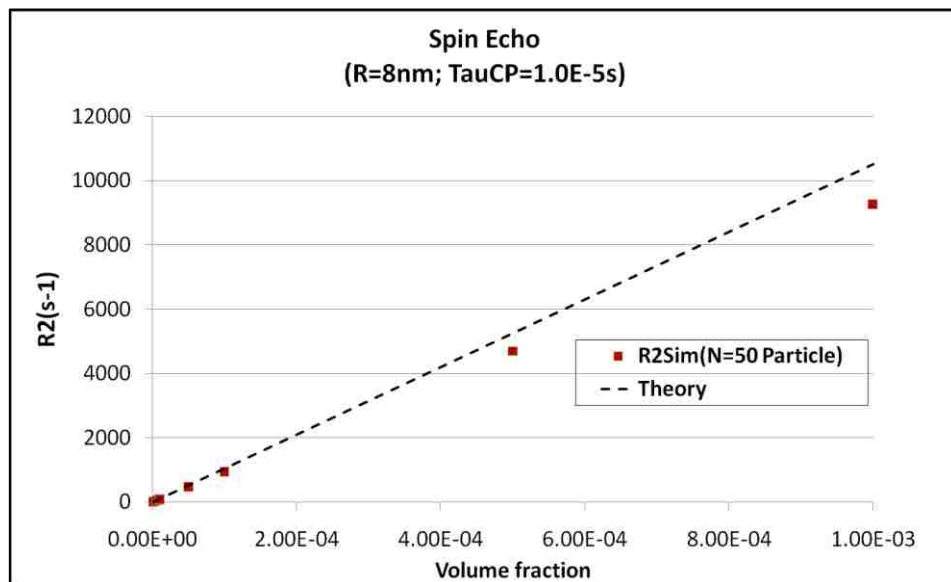
Figure 5: R_2 vs. τ_D for all motional regimes

4.2 The effect of increasing volume fraction

Volume fraction was increased gradually for the 50 SPIONs in order to investigate the effect of changing the volume fraction on both R_2 and R_2^* . This number of SPIONs was chosen as it gave an optimal values for the relaxation rates upon comparing three sets. This will be discussed in section 4.3.

The sizes of the SPIONs were equal, the radii were 8 nm and $\tau_{CP} = 1.0 \times 10^{-5}$ s. The volume fractions studied was between ($f= 1.0 \times 10^{-6}$) and ($f= 1.0 \times 10^{-3}$).

The relaxation rates increased with increasing volume fraction. Figure 6 and Figure 7 showed that both values of R_2^* and R_2 were in agreement with the theoretical values at low volume fraction. However, both R_2 and R_2^* relaxation rates did not agree with the theoretical values as the volume fraction increased beyond ($f=1.0 \times 10^{-4}$). The theory seems to overestimate the relaxation rates for increasing volume fraction in both cases. In contrast, the simulation evaluated values for R_2 and R_2^* obtained from the simulation were very near to each other over the volume fraction range in this study. The theory predicts that R_2 is equal to R_2^* in the motional averaging regime.

Figure 6: R_2^* values plotted vs. volume fractionFigure 7: R_2 values plotted vs. volume fraction

4.3 The effect of changing the number of magnetic nanoparticles

Figure 8 and Figure 9 show the effect of changing the volume fraction on the values of R_2 and R_2^* obtained from the simulation for different numbers of SPIONs. The random walk was run for 1 particle and for 10 particles, and compared with the relaxation rate values with the values obtained earlier for the 50 SPIONs in section 4.2 to check if decreasing the number of particles would yield results in better agreement with the theoretical values and with lower error at high volume fractions.

The results showed that both R_2 and R_2^* were increasing with increasing volume fraction. All the values of the simulation transverse relaxation rates obtained for the three sets matched the theoretical values at the low volume fraction (up to $f = 1.0 \times 10^{-4}$). The results were repeated and the error was estimated to confirm the trend.

Overall, there was a greater difference in the relaxation as the volume fraction increased in the values of R_2 than in the values of R_2^* . Also for higher volume fraction the relaxation increased by increasing the number of particles.

It was clear that the theory overestimates both R_2 and R_2^* . The error bars were very small, but for the (N= 1 particle) R_2^* error bars were within the theory line.

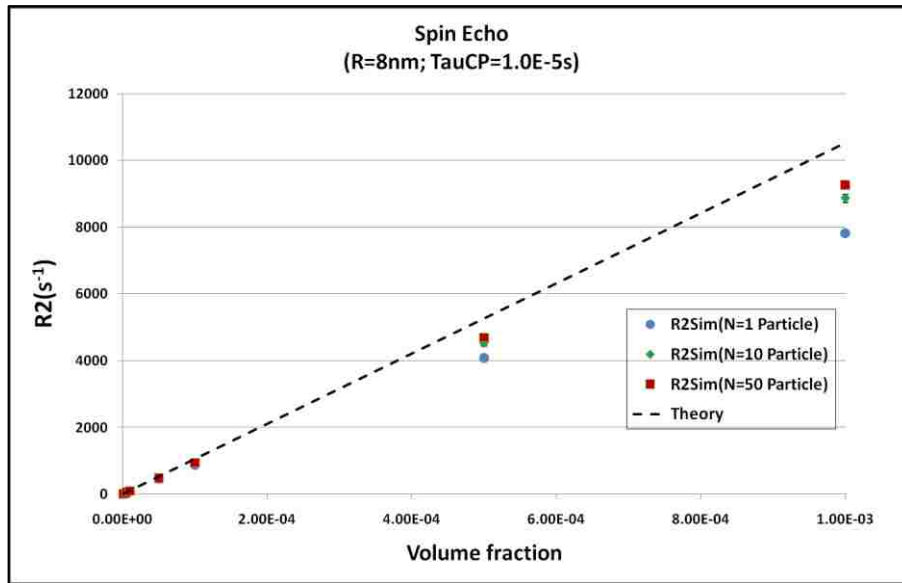


Figure 8: The effect of increasing the number of the particles on R₂

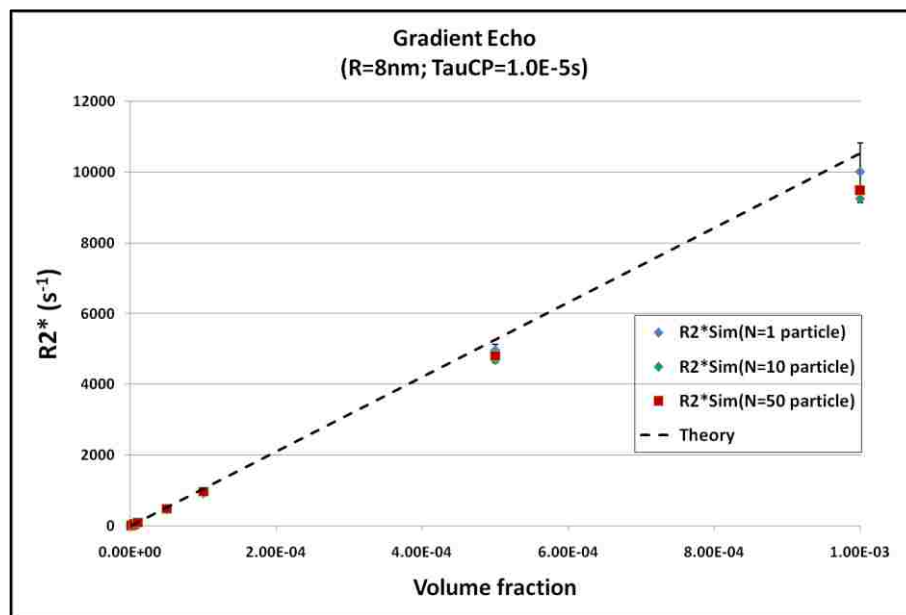


Figure 9: The effect of increasing the number of the particles on R₂*

4.4 Motional Regimes

The effect of increasing volume fraction (f) on R_2 and R_2^* was studied at different values of τ_{CP} for two sets SPIONs which have sizes that scan both regimes of MAR and SDR. The range of volume fraction was ($f = 1.0 \times 10^{-6}$ to $f=1.0 \times 10^{-3}$) for SPIONs of sizes ($R=10$ nm) and ($R=240$ nm).

4.4.1 MAR (R=10 nm)

The effect of increasing volume fraction over a range of τ_{CP} between 1.0×10^{-8} s and 5.0×10^{-5} s for 50 SPIONs was studied to explore R_2 and R_2^* simulation evaluated values dependence on both volume fraction and echo time. This simulation results are shown in Figure 12 and Figure 15. Monoexponential fitting was used to get the values of both R_2 and R_2^* for this MNP size.

4.4.2 SDR/ELR (R=240 nm)

Identical 50 SPIONs of 240 nm radii were used to scan both SDR and ELR. The range of τ_{CP} was in the range between 3.0×10^{-5} s and 1.0×10^{-3} s. Monoexponential fitting was used to get the values of R_2^* , while double exponential fitting was used to get the values of R_2 as the spin echo did not show monoexponential trend for this MNP size. Figure 10 shows the \ln of the phases accumulated by the spins for volume fraction of 1.0×10^{-6} and τ_{CP} 1.0×10^{-3} s. The linear trend in the plot confirms the monoexponential relaxation. The slope (-34.888) represents the value of R_2^* .

Figure 11 illustrates the loss of SE and GE signal due to increasing volume fraction lost under noise caused by gradient, and the loss in the echo when the echo time becomes so long so the signal dies out. This appears partially in (b) and totally in (c). The echo was neither lost in (a) nor in (d); as the echo time was shorter (a) and the volume fraction had a low value (1.0×10^{-5}) in (d).

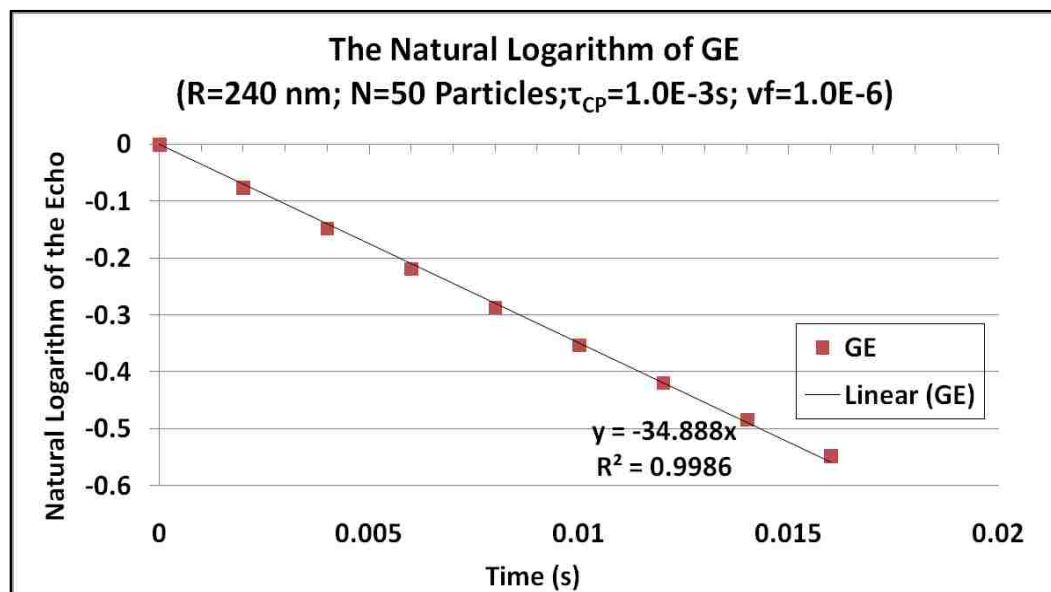
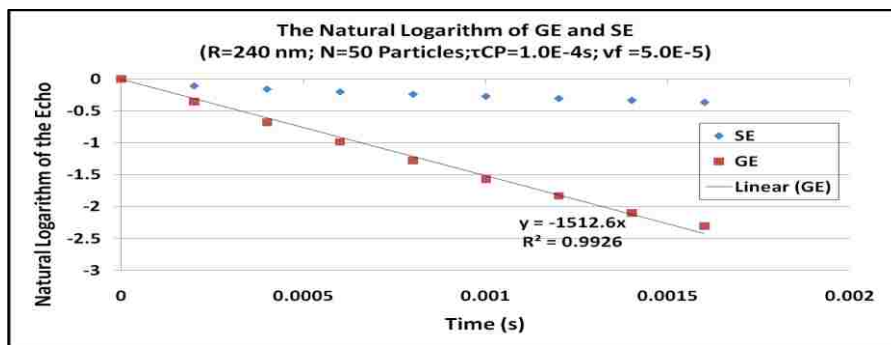
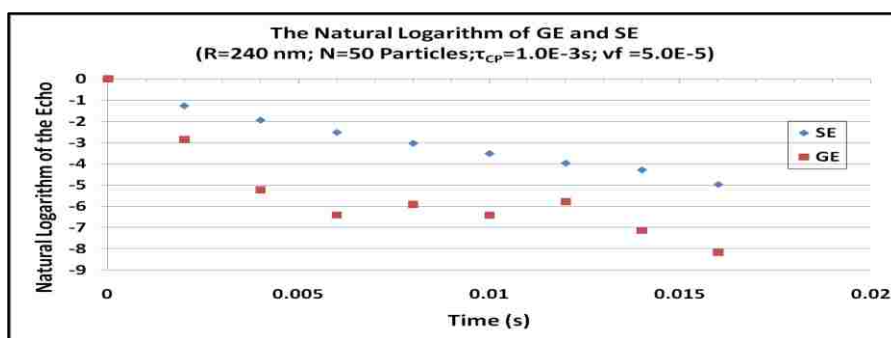


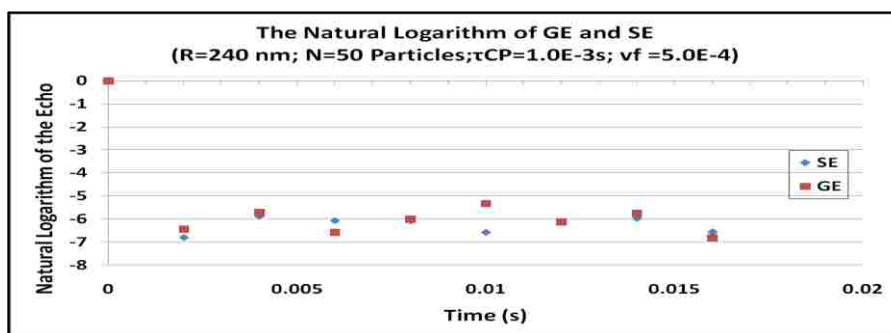
Figure 10: Values of Ln of the accumulated phase of the spins in both SE and GE at volume fraction of 1.0×10^{-6}



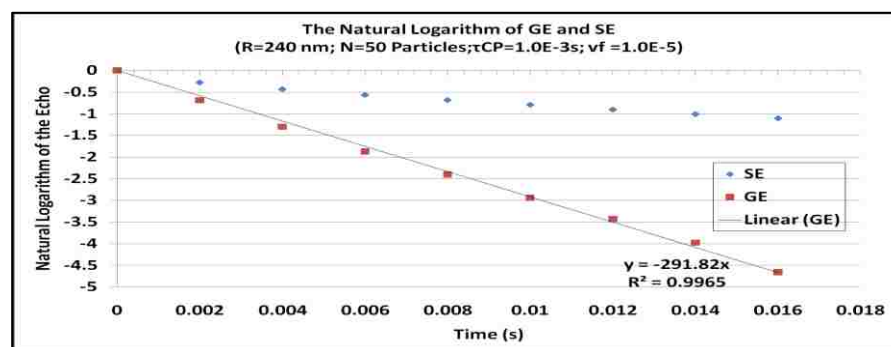
(a)



(b)



(c)



(d)

Figure 11: The natural logarithm of the phases accumulated by the 4000 spins in random walk around 50 SPIONs of radii 240 nm plotted vs. time. The parameters in each subplot are (a) $\tau_{CP} = 1.0 \times 10^{-4}s$; $f = 5.0 \times 10^{-5}$ (b) $\tau_{CP} = 1.0 \times 10^{-3}s$; $f = 5.0 \times 10^{-5}$; (c) $\tau_{CP} = 1.0 \times 10^{-3}s$; $f = 5.0 \times 10^{-4}$; (d) $\tau_{CP} = 1.0 \times 10^{-3}s$; $f = 1.0 \times 10^{-5}$.

4.4.3 The saturation effect

Increasing volume fraction caused the signal to be lost before reaching the 8th refocusing pulse. In these cases, the relaxation values were taken within the first refocusing pulses in the presence of signal for the simulation results of the 240 nm SPIONs at higher values of both echo time and volume fraction.

4.5 The effect of increasing volume fraction on R_2^* at different τ_{CP} values

The results showed that R_2^* relaxation rate in both cases of ($R=10$ nm) and ($R= 240$ nm) increased with increasing volume fraction. As the volume fraction increased, R_2^* did not agree with the theoretical values.

The effect of the echo time was not noted when the volume fraction was low. i.e. having values below (5.0×10^{-5}). On the other hand, the effect of echo time on R_2^* became prominent as the volume fraction increased beyond this limit.

The differences between each R_2^* from the theoretical values became larger as the volume fraction increases for different values of echo time, as can be seen in Figure 12 and Figure 13, for both sizes (10 nm and 240 nm).

The difference between the simulation and the theory at large τ_{CP} is larger for the 240 nm SPIONs than the difference between the simulation and the theory for the 10 nm SPIONs. Also, the values of R_2^* for the 240 nm SPIONs were obtained from an exponential decay. Whereas, the values of R_2^* for the 10 nm were obtained from monoexponential decay. It is clear from the plots that there is a monotonic relationship between both R_2 and R_2^* with the echo time.

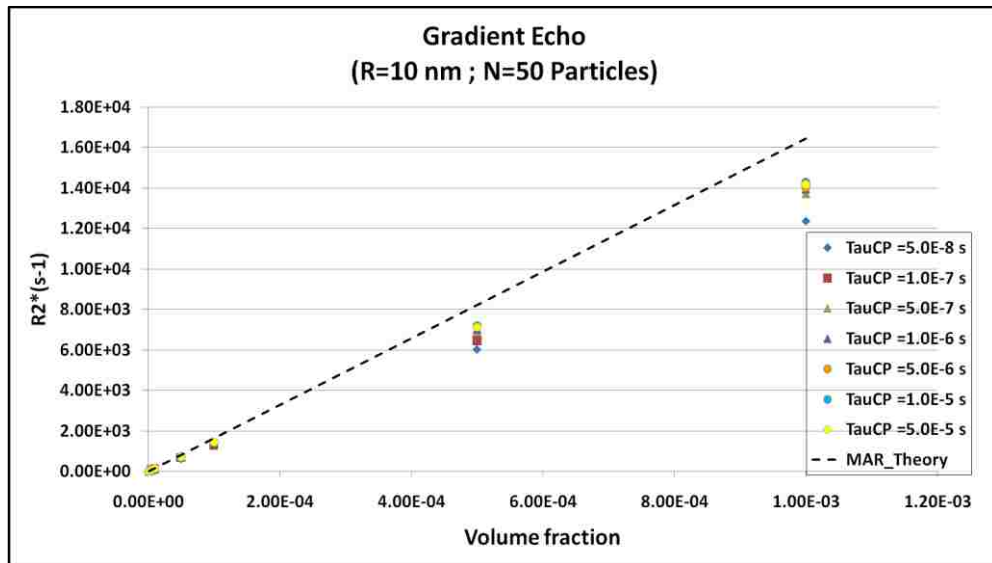


Figure 12: R_2^* vs. volume fraction at different the echo time R=10 nm

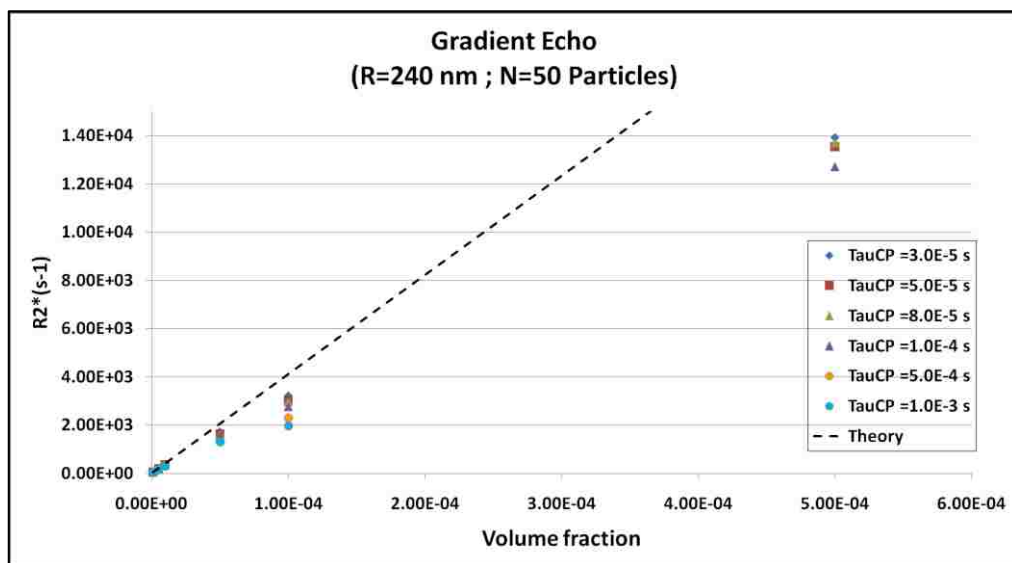


Figure 13: R_2^* values plotted against volume fraction for 50 SPIONs of 240 nm radii

4.6 The effect of increasing volume fraction on R_2 and at different τ_{CP} values

The values for R_2 are plotted against volume fraction in Figure 14 and Figure 15 for the particle sizes showed that values were increasing with increasing volume fraction with different slopes for the range of echo time in the study.

The results in Figure 14 showed that for the SPIONs of 240 nm radii, there is a direct relaxation between R_2 and the volume fraction. The increase in the slope is not monotonic with τ_{CP} .

For the case the 10 nm, as shown in Figure 15, particles showed linear increasing R_2 relaxation rate vs. volume fraction. At high values of volume fraction, the relaxation seemed to be more dependent on the echo time. Also, unlike the 240 nm SPIONs, the increase in slope is monotonic relationship.

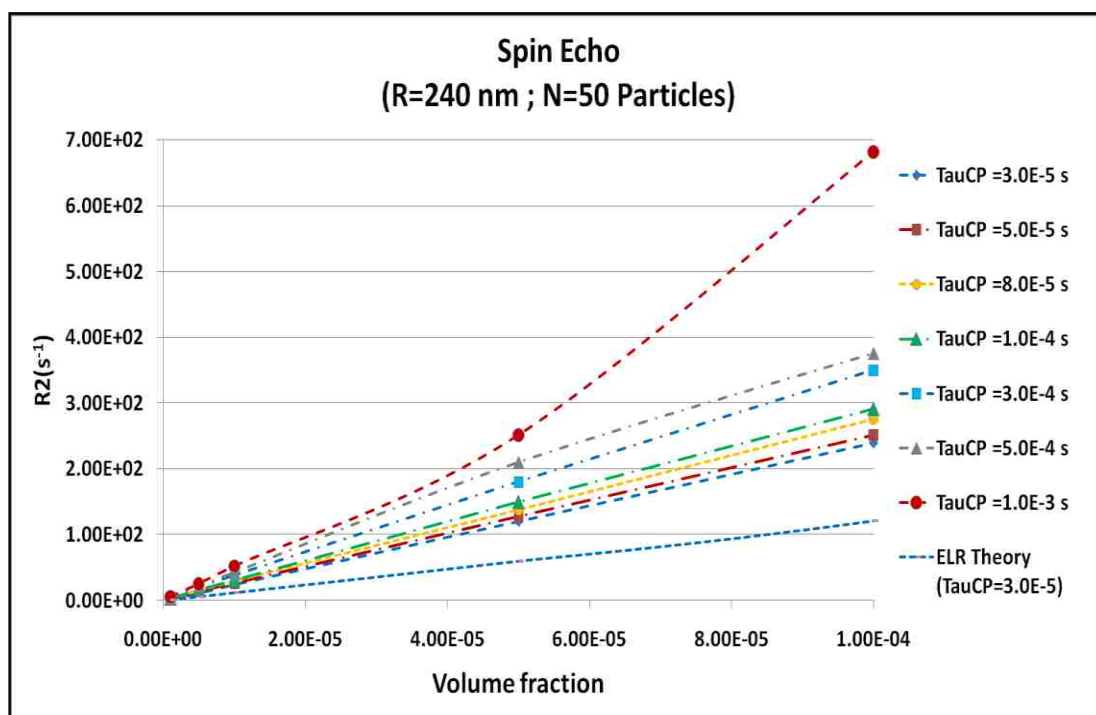


Figure 14: R_2 values plotted against volume fraction for 50 SPIONs of 240 nm radii

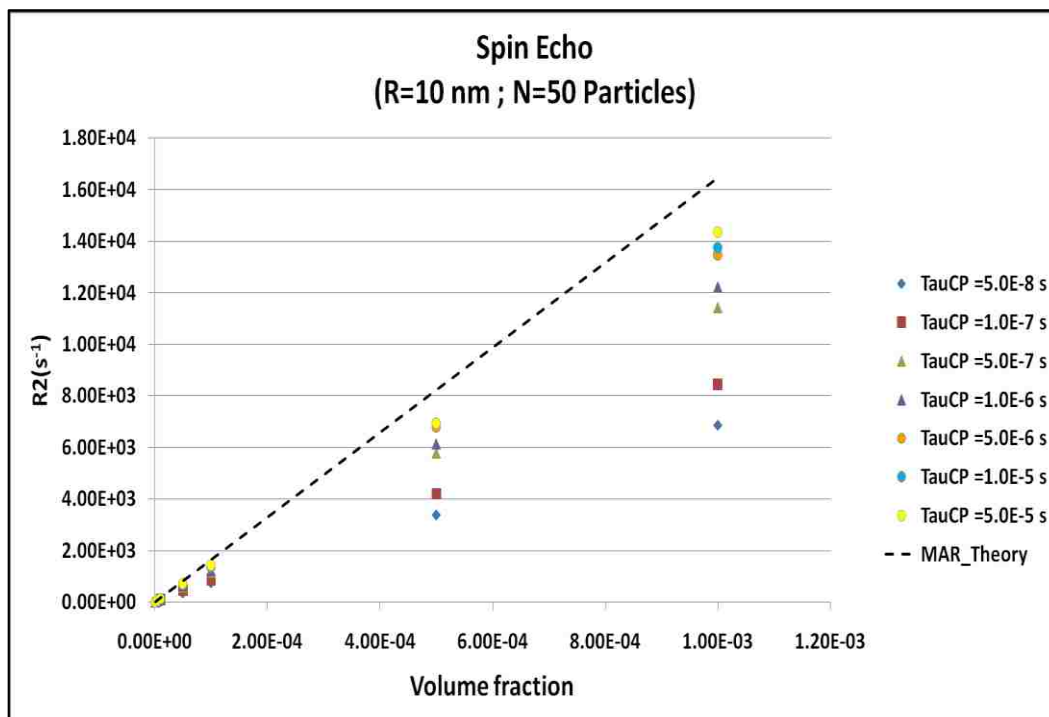


Figure 15: R_2 values plotted against volume fraction for 50 SPIONs of 10 nm radii

4.7 The effect of increasing τ_{CP} on R_2^* for different volume fractions

The results for the 240 nm SPIONs, as shown in Figure 16 shows a decrease in R_2^* with increasing echo time. The values R_2^* the relaxation could not be evaluated for the volume fraction above ($f = 1.0 \times 10^{-4}$) above an echo time of (3.0×10^{-4} s). On the other hand, the results for the 10 nm SPIONs (Figure 16) showed sharp increase in the gradient echo relaxation rate for values of echo time below (2.0×10^{-6} s), then the R_2^* remained steady by increasing the echo time. Higher the relaxation rates were higher for the higher volume fractions (Figure 17).

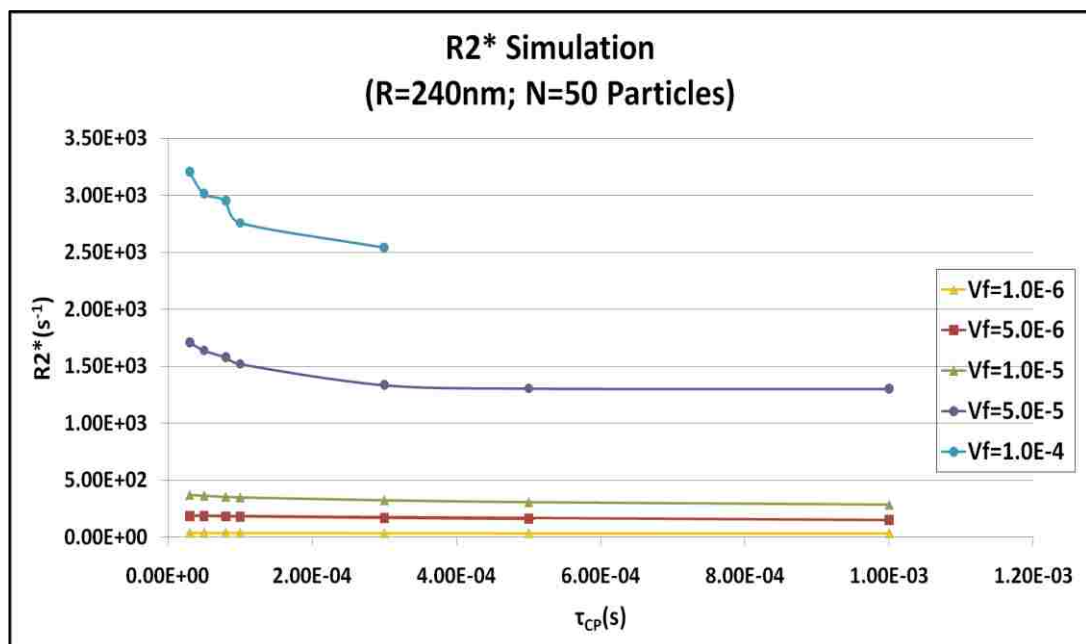


Figure 16: R_2^* values plotted against volume fraction for 50 SPIONs of 240 nm radii

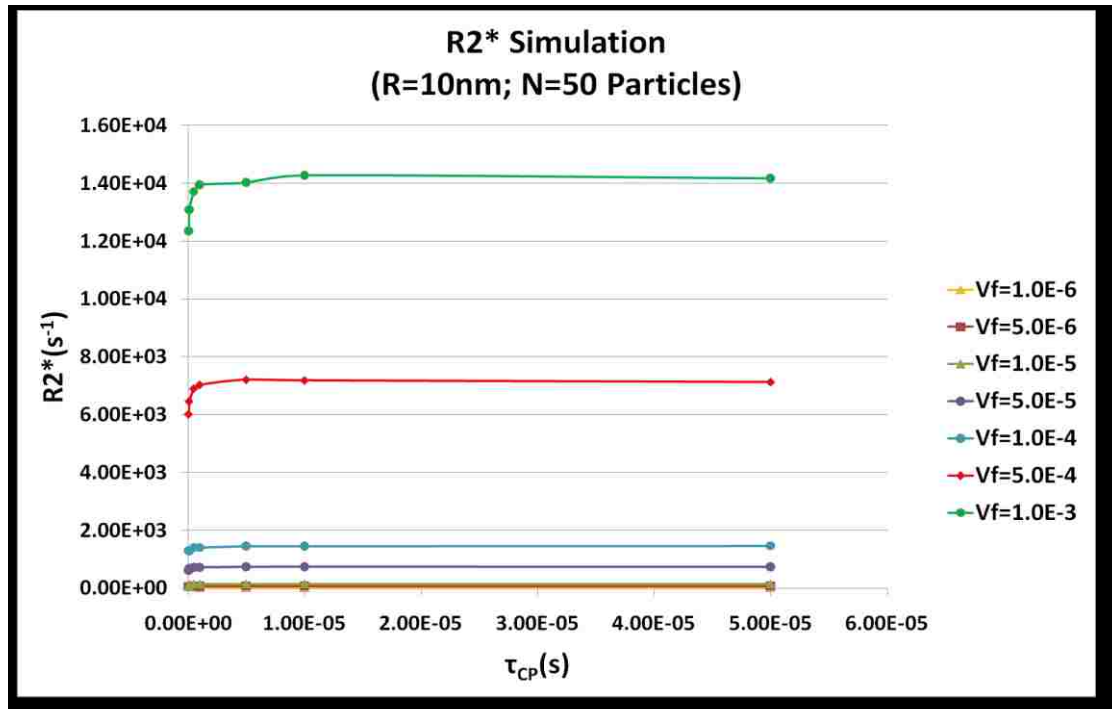


Figure 17: R_2^* values plotted against volume fraction for 50 SPIONs of 10 nm

4.8 The effect of increasing τ_{CP} on R_2 for different volume fractions

The results for the 10 nm SPIONs (Figure 18) showed that the spin-echo increased quickly for echo times between $(1.0 \times 10^{-6}s)$ and $(1.0 \times 10^{-5}s)$. The spin echo rate had a different trend and became steady. R_2 values plotted against τ_{CP} for the 240 nm particle. Figure 19 showed an increase in the spin-echo relaxation rates.

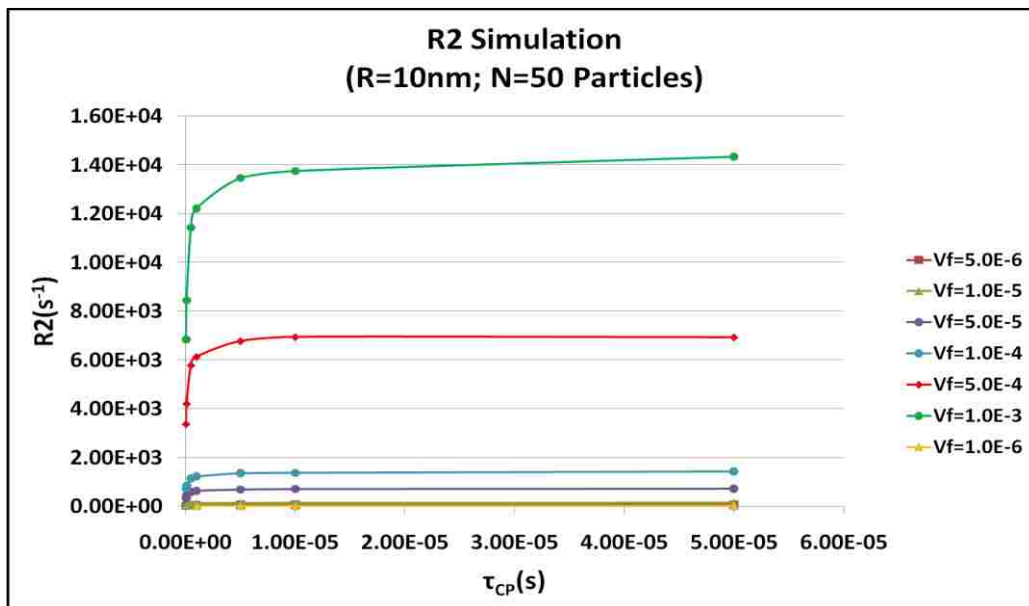


Figure 18: R_2 values plotted against volume fraction for 50 SPIONs of 10 nm

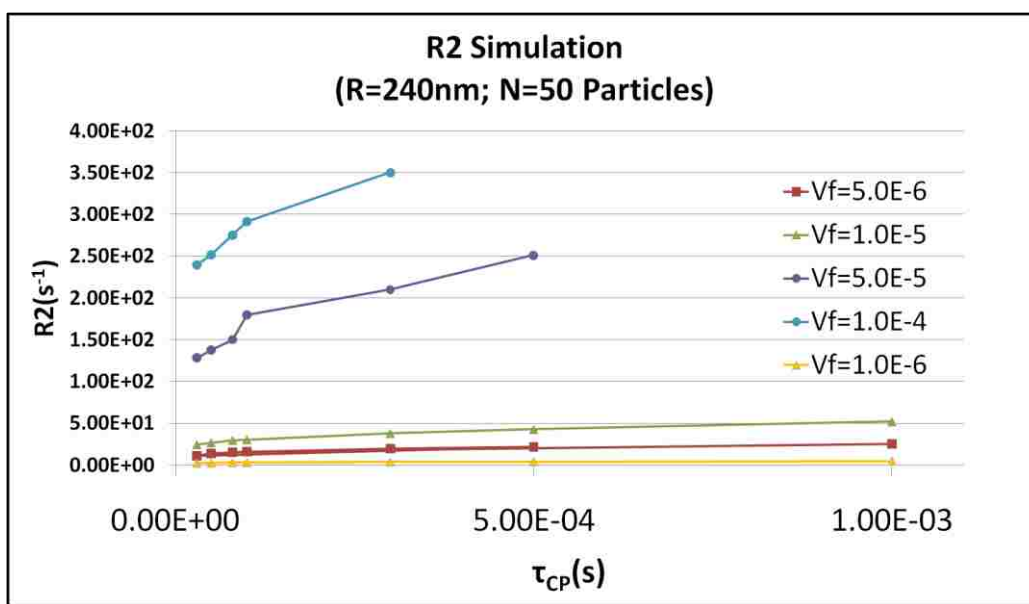


Figure 19: R_2 values plotted against volume fraction for 50 SPIONs of 240 nm

4.9 The effect of increasing τ_{CP} on the slope of (R_2 and R_2^* vs. the volume fraction)

The slope for the transverse relaxation rates vs. volume fraction (as derived from Figures 12-15) over the echo time range as seen in Figure 20 increase in the values for the values of τ_{CP} less than $(1.0 \times 10^{-6}s)$. The slopes reached steady

values above ($\tau_{CP} = 1.0 \times 10^{-6}$ s). Figure 20 compares the slopes in sense of the magnitude and showed that the gradient-echo vs. volume fraction slope was higher than the spin-echo vs. volume fraction slope for all the values of τ_{CP} in this study for this MNP size.

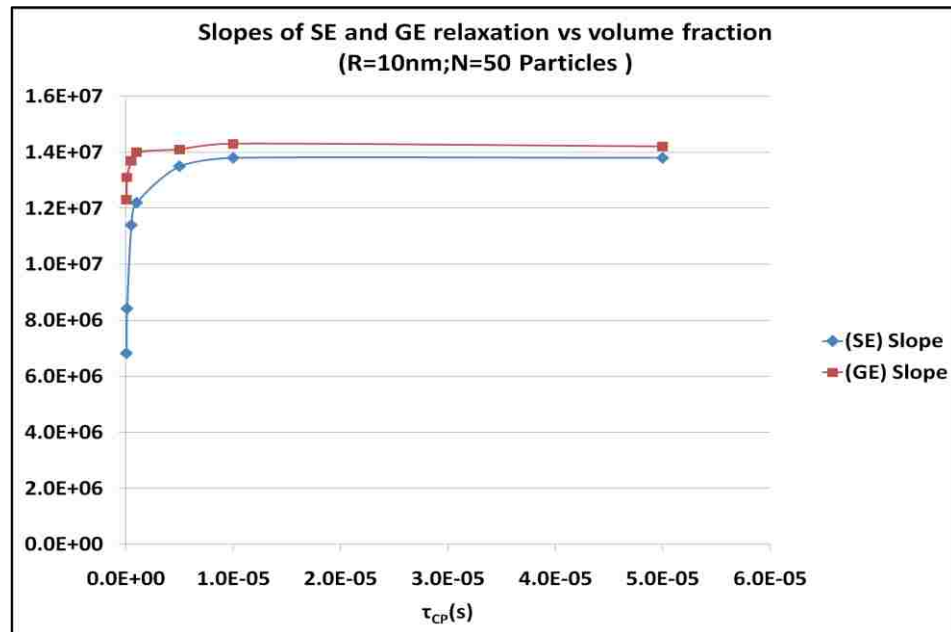


Figure 20: Comparing Slopes of (R_2^* vs.f) and (R_2 vs.f) vs. τ_{CP} ; R=10 nm

Figure 21, shows the slopes for the spin echo and gradient echo relaxation vs. the echo time for 240 nm SPIONs. The plot shows that there were greater slopes for (R_2^* vs.f) than the slopes (R_2 vs.f) for all echo-time values studied.

There has been a single sharp increase in the gradient echo vs. volume fraction slope at ($\tau_{CP} = 5.0 \times 10^{-5}$ s) reaching a maximum at ($\tau_{CP} = 8.0 \times 10^{-5}$ s) followed by decrease till ($\tau_{CP} = 1.0 \times 10^{-4}$ s). This contributes to overlapping of the fields of the SPIONs and coming to saturation afterwards. It was shown in the plot

that the spin echo vs. volume fraction slope had a slight increase at the same τ_{CP} values.

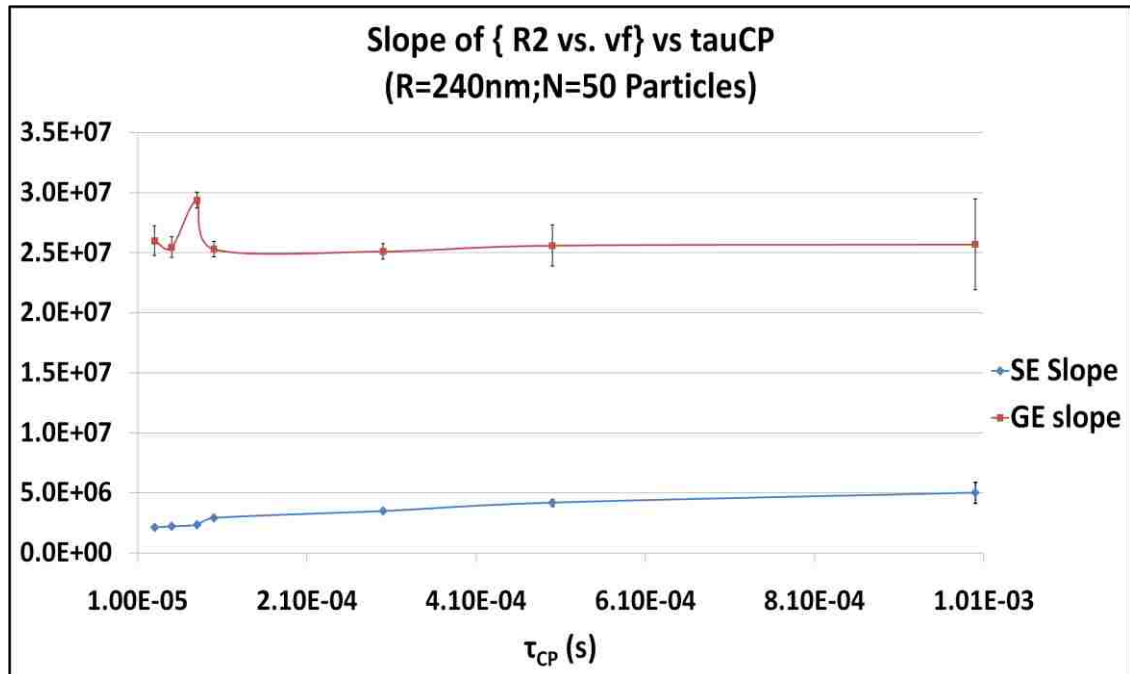


Figure 21: Comparing Slopes of (R_2^* vs.f) and (R_2 vs.f) vs. τ_{CP} ; R=240 nm

4.10 3D Graphs.

In this section, 3-D display of the results for the two cases of transverse relaxation and two cases of particle sizes are displayed.

The gradient echo dependence on both volume fraction and echo time for both MNP sizes are shown in Figure 22. The subplot (a) shows the R_2 simulation values plotted against τ_{CP} and volume fraction for the 10 nm SPIONs, while (b) shows the simulation values for R_2^* of the same size. Subplots (c) and (d) show the simulation values for R_2 and R_2^* for the 240 nm SPIONs. Part of the graph (corresponding of the high value of volume fraction and for long echo time) is missing in the case of the 240 nm SPIONs as the signal was lost for higher values of volume fractions and longer echo time.

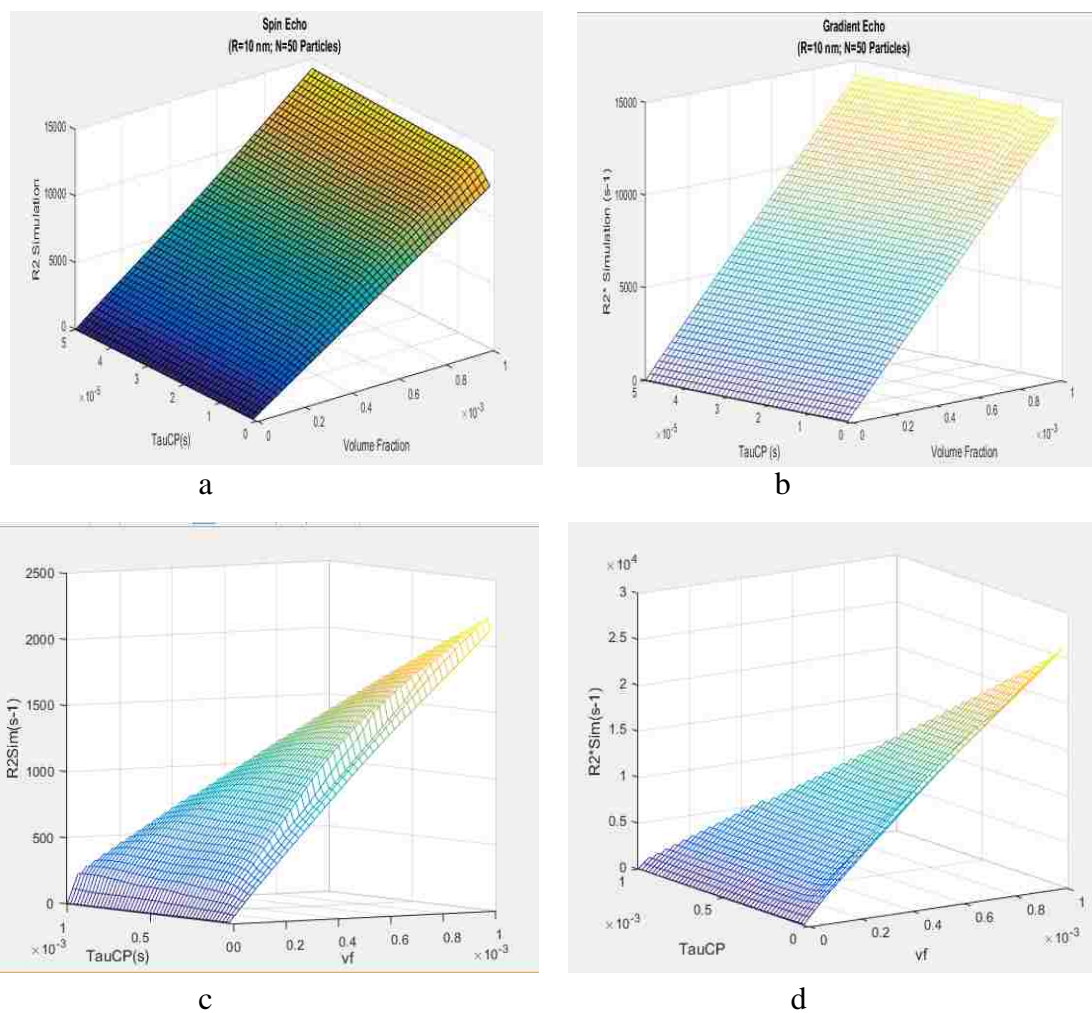


Figure 22: 3D Representation of R2 and R2* against volume fraction and echo time

Chapter 5: Discussion and Conclusion

The work in this research contributes to a better understanding of volume fraction influence on the transverse relaxation of SPIONs over increasing values of volume fraction. This analysis is important to get a better understanding of the mechanism of relaxation and predict relaxation rates under conditions existing in when nanoparticles cluster inside biological tissues or trapped inside cells.

One example is Natural sedimentation effects and large magnetic dipolar interactions under in vivo environment or heating as in hyperthermia conditions. This means that volume fraction of superparamagnetic nanoparticles would increase to a limit which could not be predicted by the existing theoretical models.

The transverse relaxation rates were studied systematically both for 10 nm and 240 nm particle's sizes.

5.1 The transverse relaxation at high concentration

At low volume fraction the simulated R_2 and R_2^* agreed with the theory. The match with the theory was lost for values of R_2 and R_2^* as the volume fraction increased, as demonstrated in Figure 6 and Figure 7. The disagreement was expected as the theoretical models were built for very small SPIONS which are very far from each other, and this can be satisfied only under very low volume fraction.

5.2 The effect of the echo time on transverse relaxation on the 10 nm SPIONs

The echo time was an important parameter as the volume fraction increases, i.e. changing the echo time has an effect on the values of transverse relaxation rates, as shown in Figure 12 and Figure 15. However, the spread of the values of R_2 was wider than R_2^* as the volume fraction increased for the same range of echo time.

At low volume fraction, the effect of echo time was not noted for this particle size for the small volume fraction and all the values of both R_2 and R_2^* were very near and in agreement with the theoretical values.

The slopes of R_2 vs. volume fraction and R_2^* vs. volume fraction were studied systematically. Both R_2 and R_2^* increased steadily with increasing volume fraction. The value for R-squared was 1 for all the fitting graphs of 10 nm SPIONs. Whereas, R-squared was between 0.99 and 1 for the 240 nm SPIONs. Table (1) and Table (2) illustrate the trends of R_2 and R_2^* simulation values with increasing volume fraction for the particle sizes in this study and shows the R-squared value for each slope fitting.

Table 1: The values of the relaxation vs. f slopes and their R-squared values for 240 nm SPIONs

$\tau_{CP}(s)$	Slope of R_2 vs. f	R-squared	Slope of R_2^* vs. f	R-squared
3.0×10^{-5}	2.13×10^6	0.99	2.60×10^7	0.99
5.0×10^{-5}	2.22×10^6	0.99	2.55×10^7	1.00
8.0×10^{-5}	2.35×10^6	0.99	2.94×10^7	0.99
1.0×10^{-4}	2.92×10^6	1.00	2.53×10^7	1.00
3.0×10^{-4}	3.49×10^6	1.00	2.51×10^7	0.99
5.0×10^{-4}	4.19×10^6	1.00	2.56×10^7	0.99
1.0×10^{-3}	5.02×10^6	0.99	2.57×10^7	1.00

Table 2: The values of the relaxation vs. f slopes and their R-squared values for 10 nm SPIONs

$\tau_{CP}(s)$	Slope of R_2 vs. f	R-squared	Slope of R_2^* vs. f	R-squared
5.0×10^{-8}	6.83×10^6	1.00	1.23×10^7	1.00
1.0×10^{-7}	8.42×10^6	1.00	1.31×10^7	1.00
5.0×10^{-7}	1.14×10^7	1.00	1.37×10^7	1.00
1.0×10^{-6}	1.22×10^7	1.00	1.40×10^7	1.00
5.0×10^{-6}	1.35×10^7	1.00	1.41×10^7	1.00
1.0×10^{-5}	1.38×10^7	1.00	1.43×10^7	1.00
5.0×10^{-5}	1.38×10^7	1.00	1.42×10^7	1.00

The slopes of R_2 vs. volume fraction and R_2^* vs. volume fraction were increasing constantly with the values of echo time between ($5.0 \times 10^{-8}s$) and ($5.0 \times 10^{-6}s$) as shown in Figure 20. Beyond the echo time ($\tau_{CP} = 5.0 \times 10^{-6}s$), both R_2 and R_2^* came to a plateau. At this echo time point the both (slopes of R_2 and R_2^* vs. volume fraction) vs. echo time became independent from the echo time and near to each other. Still the slope of (R_2^* vs. volume fraction) is higher than that of that of R_2 .vs volume fraction.

It seems that it could be as the echo time becomes close to diffusion time, then the transverse relaxation will become dependent on the echo time. It was not possible to get the transverse relaxation values for volume fraction $\sim 10^{-6}$ in this domain, but it was possible to get the relaxation for volumes fractions in the order of $\sim 10^{-5}$. The decrease to the order near the diffusion time needs to be studied in the future.

Using the random walk to get the transverse relaxation for SPIONs at this size would require excessive calculations as each spin would require to do around 10^6 jumps for τ_{CP} in the order of 10^{-4} s, and even around 10^7 jumps for τ_{CP} in the order of 10^{-3} s. This may be done in the future work upon the availability of more powerful computation hardware.

5.3 The effect of the echo time on transverse relaxation on the 240 nm

Although the theory is still unable to predict the values of R_2 and R_2^* at high volume fraction for this size of SPIONs, (as shown in Figure 13 and Figure 14), the simulation values showed that R_2 and R_2^* increased steadily with increasing volume fraction. There has been a different slope for each value of the echo-time.

The slope of (R_2 and R_2^* vs. volume fraction) vs. the echo time was studied. The value of R_2 slope kept increasing with increasing τ_{CP} as shown in Figure 21. The relation between slope and the echo time for the 240 nm SPIONs seems to be linear, i.e. the values for τ_{CP} (3.0×10^{-5} , 5.0×10^{-5} , and 8.0×10^{-5}) had their own linear trend. There was a peak between ($\tau_{CP} = 8.0 \times 10^{-5}$) and ($\tau_{CP} = 1.0 \times 10^{-4}$). This needs to be investigated further to rule out any simulation errors

although the calculation was repeated four times and results were self-consistent. The relation between R_2 and took the linear shape again beyond this point.

With reference to Figure 24, the slope of (R_2^* vs. volume fraction) has a hump between ($\tau_{CP} = 5.0 \times 10^{-5}$) and ($\tau_{CP} = 1.0 \times 10^{-4}$) which has a maximum at ($\tau_{CP} = 8.0 \times 10^{-5}$), comparing with the slope of (R_2 vs. volume fraction). This was the same time interval for the hop. The simulation was repeated four times and the results assured that pattern came from the physical phenomenon. The error bars showed increasing values as τ_{CP} increased beyond (3.0×10^{-5} s).

This shows that the slope of (R_2^* vs. volume fraction) is independent of τ_{CP} and this opens the door towards the possibility of other factors causing this change in the slope at this certain time interval. However, the slope of (R_2^* vs. volume fraction) was higher than the slope of (R_2 vs. volume fraction) by around 85% to 92% over the echo time range studied.

The 240 nm SPIONs gradient echo signal was strong and the relaxation values could be obtained from the simulation for the range of volume fraction between (1.0×10^{-6} and 1.0×10^{-3}) when τ_{CP} was on the order of $\sim 10^{-5}$ s. i.e. ($\tau_{CP} = 3.0 \times 10^{-5}$ s and 5.0×10^{-5} s). One example is shown in Figure 10 for a volume fraction of (1.0×10^{-6}).

However, the signal was lost under noise for higher values of volume fraction for longer echo time as shown in Figure 11. The simulation relaxation values were for the volume fraction ranging from (1.0×10^{-6} to 5.0×10^{-4}) for echo time of order $\sim 10^{-4}$ s. The range of volume fraction at which the transverse relaxation could

be evaluated were between (1.0×10^{-6} to 5.0×10^{-5}) when the echo time became of the order of $\sim 10^{-3}$ s.

5.4 Conclusion

The work in this study used Mont Carlo random walk to evaluate the transverse relaxation rates influence on SPIONs at higher volume fractions. The two case studies included in this work were for 10 nm and 240 nm SPIONs.

For both sizes of SPIONs the transverse relaxation increased linearly with increasing volume fraction for both cases. Under different values of echo time, the relation between the transverse relaxation rates of SPIONs and the increasing volume fraction kept linear. However, the slopes $(\frac{dR_2}{df})$ and $(\frac{dR_2^*}{df})$ were changing for each echo time.

Running the simulation multiple times and getting the error bars confirmed that the change in the slope of the transverse relaxation vs. volume fraction was originating from the physical phenomenon.

The slopes $(\frac{dR_2}{df})$ and $(\frac{dR_2^*}{df})$ for the 10 nm SPIONs increased sharply as the echo time increased and came to a plateau after a critical echo time of (5.0×10^{-6} s). For both R_2 and R_2^* . In contrast, the values of $(\frac{dR_2}{df})$ for the 240 nm SPIONs increased steadily by increasing the echo time as long as the signal can be detected and was limited by the noise. On the other hand $(\frac{dR_2^*}{df})$ increased reaching a maximum and decreased with echo time the maximum was at the echo time (8.0×10^{-5} s). It was noted that this echo time there was a saturation in magnetic field and starting to lose the signal at high volume fractions.

Work on this initial study needs to continue in order to quantify accuracy of calculations in more detail and to extend the range of echo times studied particularly for the ELR regime. Computation times are excessive at the moment. Functional fitting can also be applied to build up a model for the dependence of transverse relaxation rate on volume fractions and echo times.

The smaller simulated values for R_2 and R_2^* can be explained in terms of smaller magnetic field gradients generated by the smaller distances separating the MNPs (at large volume fractions). This should not be confused with the large magnitudes of magnetic field strengths (i.e. not gradients). The current theory is based on small volume fraction which means that fields from individual particles do not overlap significantly, especially in view of $(1/r^3)$ field dependence. Numerical simulation, of course, does not suffer from this factor and add up contributions from all particles irrespective of their fraction. The theoretical models need to take this into account.

References

- [1] Ramsey, N.F., *Early history of magnetic resonance*. Physics in perspective, 1999. **1**(2): p. 123-135.
- [2] Carr, H.Y. and E.M. Purcell, *Effects of diffusion on free precession in nuclear magnetic resonance experiments*. Physical review, 1954. **94**(3): p. 630-638.
- [3] Geva, T., *Magnetic resonance imaging: historical perspective*. J Cardiovasc Magn Reson, 2006. **8**(4): p. 573-80.
- [4] Liang, Z.-P. and P.C. Lauterbur, *Principles of magnetic resonance imaging: a signal processing perspective*. 2000: SPIE Optical Engineering Press.
- [5] Rummeny, E.J., P. Reimer, and W. Heindel, *MR imaging of the body*. 2009.
- [6] Hahn, E.L., *Spin echoes*. Physical review, 1950. **80**(4): p. 580-594.
- [7] Meiboom, S. and D. Gill, *Modified spin-echo method for measuring nuclear relaxation times*. Review of scientific instruments, 1958. **29**(8): p. 688-691.
- [8] Burtea, C., et al., *Contrast agents: magnetic resonance*, in *Molecular imaging I*. 2008, Springer. p. 135-165.
- [9] Jensen, J. and R. Chandra, *NMR relaxation in tissues with weak magnetic inhomogeneities*. Magnetic Resonance in Medicine: An Official Journal of the International Society for Magnetic Resonance in Medicine, 2000. **44**(1): p. 144-156.
- [10] Brooks, R.A., F. Moyny, and P. Gillis, *On T2-shortening by weakly magnetized particles: the chemical exchange model*. Magnetic Resonance in Medicine: An Official Journal of the International Society for Magnetic Resonance in Medicine, 2001. **45**(6): p. 1014-1020.
- [11] Issa, B., *Reduction of T2 Relaxation Rates due to Large Volume Fractions of Magnetic Nanoparticles for All Motional Regimes*. Applied Sciences, 2018. **8**(1): p.101-9.
- [12] Ayant, Y., et al., *Calcul des densités spectrales résultant d'un mouvement aléatoire de translation en relaxation par interaction dipolaire magnétique dans les liquides*. Journal de Physique, 1975. **36**(10): p. 991-1004.
- [13] Yablonskiy, D.A. and E.M. Haacke, *Theory of NMR signal behavior in magnetically inhomogeneous tissues: the static dephasing regime*. Magn Reson Med, 1994. **32**(6): p. 749-63.

- [14] Brown, R.J., *Distribution of fields from randomly placed dipoles: free-precession signal decay as result of magnetic grains*. Physical Review, 1961. **121**(5): p. 1379-1382.
- [15] Gillis, P., F. Moyny, and R.A. Brooks, *On $T(2)$ -shortening by strongly magnetized spheres: a partial refocusing model*. Magn Reson Med, 2002. **47**(2): p. 257-63.
- [16] Chen, D.-X., et al., *Experimental study on $T2$ relaxation time of protons in water suspensions of iron-oxide nanoparticles: Effects of polymer coating thickness and over-low $1/T2$* . Journal of Magnetism and Magnetic Materials, 2010. **322**(5): p. 548-556.
- [17] Weisskoff, R.M., et al., *Microscopic susceptibility variation and transverse relaxation: theory and experiment*. Magn Reson Med, 1994. **31**(6): p. 601-10.
- [18] Brown, R.W., et al., *Magnetic resonance imaging: physical principles and sequence design*. 2014: John Wiley & Sons.
- [19] Muller, R.N., et al., *Transverse relaxivity of particulate MRI contrast media: from theories to experiments*. Magn Reson Med, 1991. **22**(2): p. 178-82.
- [20] Boxerman, J.L., et al., *MR contrast due to intravascular magnetic susceptibility perturbations*. Magnetic resonance in medicine, 1995. **34**(4): p. 555-566.
- [21] Matsumoto, Y. and A. Jasanoff, *$T2$ relaxation induced by clusters of superparamagnetic nanoparticles: Monte Carlo simulations*. Magn Reson Imaging, 2008. **26**(7): p. 994-8.